Prediction of capillary hysteresis in a porous material using lattice-Boltzmann methods and comparison to experimental data and a morphological pore network model

B. Ahrenholz [a], J. Tölke [a,*], P. Lehmann [b,1], A. Peters [c], A. Kaestner [b,2], M. Krafczyk [a], W. Durner [c]

[a] Institute for Computational Modeling in Civil Engineering, TU Braunschweig, Pockelsstrasse 3, Germany
[b] Institute of Terrestrial EcoSystems, ETH Zürich, Universitätstrasse 16, Switzerland
[c] GeoEcology and Soil Science, TU Braunschweig, Langer Kamp 19c, Germany

ARTICLE INFO

ABSTRACT

In this work we use two numerical methods which rely only on the geometry and material parameters to predict capillary hysteresis in a porous material. The first numerical method is a morphological pore network (MPN) model, where structural elements are inserted into the imaged pore space to quantify the local capillary forces. Then, based on an invasion–percolation mechanism, the fluid distribution is computed. The second numerical method is a lattice-Boltzmann (LB) approach which solves the coupled Navier–Stokes equations for both fluid phases and describes the dynamics of the fluid/fluid interface. We have developed an optimized version of the model proposed in [Tölke J, Freudiger S, Krafczyk M. An adaptive scheme for LBE multiphase flow simulations on hierarchical grids, Comput. Fluids 2006;35:820–30] for the type of flow problems encountered in this work. A detailed description of the model and an extensive validation of different multiphase test cases have been carried out. We investigated pendular rings in a sphere packing, static and dynamic capillary bundle models and the residual saturation in a sphere packing.

A sample of 15 mm in diameter filled with sand particles ranging from 100 to 500 μm was scanned using X-rays from a synchrotron source with a spatial resolution of 11 μm. Based on this geometry we computed the primary drainage, the first imbibition and the secondary drainage branch of the hysteresis loop using both approaches. For the LB approach, we investigated the dependence of the hysteresis loop on the speed of the drainage and the imbibition process. Furthermore we carried out a sensitivity analysis by simulating the hysteretic effect in several subcubes of the whole geometry with extremal characteristic properties. The predicted hysteretic water retention curves were compared to the results of laboratory experiments using inverse modeling based on the Richards equation.

A good agreement for the hysteresis loop between the LB and MPN model has been obtained. The primary and secondary drainage of the hysteresis loop of the LB and MPN model compare very well, and also the experimental results fit well with a slight offset of 10% in the amplitude. Differences for the first imbibition have been observed, but also large differences between two different experimental runs have been observed.

© 2008 Elsevier Ltd. All rights reserved.

1. Introduction

In multiphase flow systems of two immiscible phases like air and water in a porous medium like a soil the flow and transport properties depend on the amount and the spatial distribution of the phases within the pore space. On the pore scale the phase distribution is controlled by the capillary forces depending on pore size, surface tension, and wettability. For that reason, the relationship between capillary pressure and liquid saturation (P_c–S_w relationship) is of high importance for the prediction of water flow and solute transport. Unfortunately, this relationship is ambiguous and depends on the preceding wetting and drainage processes. This phenomenon is denoted as hysteresis and was first documented by Haines in [2]. It is caused by different pore structures relevant for drainage and wetting processes. While the drainage of a large pore body may be prevented by surrounding small pore throats, the wetting of fine pores above a large pore is hampered by the weak capillary forces in the wide body. Additional hysteresis effects are caused by a difference in advancing and receding

* Corresponding author.
E-mail address: toelke@irmb.tu-bs.de (J. Tölke).
[1] Now at the Laboratory of Soil and Environmental Physics, EPF Lausanne.
[2] Now at Varian Medical Systems, Imaging Laboratory GmbH, Baden-Dättwil.

contact angle [3] and the inclusion of air in a first wetting process. Due to the inclusion of air in a wetting process, the water saturation after the primary drainage of a completely saturated porous medium remains smaller than the porosity for any following wetting processes. After a few drainage and wetting cycles, two bounding curves, denoted as main wetting and main drainage branch, can be determined. All processes within these bounding curves are denoted as scanning curves. To model water flow and solute transport correctly, the hysteretic relationship between capillary pressure and fluid saturation must be taken into account [4,5]. To quantify the hysteresis and the scanning curves, different approaches can be distinguished. On the macroscopic scale, the shape of the scanning curves can be deduced from the main wetting and drainage curves. With such a similarity or scaling approach, the shape of any scanning curve can be described [6–8]. While most approaches are based on the main drainage and wetting curve, it is possible to compute the whole hysteresis loop based on a single main curve [9]. In addition to these scaling approaches, two new descriptions on the macroscale based on the hysteron (the simplest hysteretic system described by an operator [10]) and the quantification of the continuous and non-continuous fluid phases [11] were recently introduced.

Secondly, the range of liquid saturation as a function of capillary pressure for wetting and drainage processes can be determined using pore network models. With a pore model consisting of a pore-body and a pore-throat distribution, the hysteresis of the hydraulic functions can be reproduced. The first pore network approaches were limited to cylindrical pore throats on a rectangular lattice [12]. To enhance the flexibility and to develop more realistic pore network models, different throat shapes [13] and other lattice types [14] were introduced. The drawback of these approaches is the uncertainty of the pore-throat and pore-body distribution function which are obtained from fitting, based on measured retention functions.

Alternatively, the pore size distribution can be deduced from images of the pore space. In Øren et al. [15] the reconstructed pore space is transformed into a pore network that is used as input to a two-phase network model. Based on this work Valvatne et al. [16] constructed a network with the same topology as a scanned sandstone sample and modified the size distribution to obtain the same permeability. To apply this network to other media, the main drainage branch must be fitted to describe the wetting branch.

Finally, to predict the hysteresis loops without any fitting based on the measured pore space geometry, a direct numerical simulation of the two-phase Stokes problem can be performed. A suitable method for this task is the lattice-Boltzmann method. Pan et al. [17] applied successfully a lattice-Boltzmann approach based on the Shan–Chen [18] multiphase extension for a packing of glass beads and compared the results to experiments. Nevertheless this approach needs numerical experiments to determine the material parameters. In a later study [19] the focus moved to the determination of relative permeabilities. By using a multiple-relaxation-time (MRT) lattice-Boltzmann approach, more realistic capillary numbers could be reproduced. In [20] the primary drainage curve (without hysteretic effects) for a porous medium was simulated by a lattice-Boltzmann approach. The medium consisted of sintered glass and the geometry was obtained by tomography. The LB results were compared to the results of a full-morphological and a pore network model and a good agreement for the three models was observed. However, these results have not been compared to experimental data.

In this study we use a MPN model and an LB approach to predict hysteresis in the capillary pressure–saturation relationship for the measured pore structure of a sand sample. The LB approach is based on the multiple-relaxation-time (MRT) model with an optimized multiphase extension given in [1] and further optimized

for Stokes flow in porous media. This approach permits higher viscosity ratios and lower capillary numbers than previous LB multiphase extensions. To obtain a geometric representation suitable for the LB solver, the surface of the sand particles was reconstructed from the voxel matrix by a marching-cube algorithm and the description of the fluid behavior at the solid walls was improved by the accurate determination of the distance of the fluid nodes to the particle boundaries [21]. Also the numerical resolution of the setups was higher as in previous studies. An extensive validation for the model developed has been carried out. Complex test cases like pendular rings, a (dynamic) capillary tube bundle and the residual water saturation in a periodic array of spheres are set up and analyzed in detail.

We compare our predictions for the capillary hysteresis using the MPN and LB model to laboratory measurements, where inverse modeling based on the Richards equation was applied to compute the drainage and imbibition curves. In addition, a few equilibrium states between water saturation and capillary pressure were analyzed to validate the results of the inverse modeling.

Furthermore we carried out a sensitivity analysis by simulating the hysteresis in several subcubes of the whole geometry with extremal characteristic properties.

The paper is organized as follows: In Section 2 the laboratory experiments and the methods to determine the hysteresis curves by an inverse fitting procedure are described. Section 3 introduces the morphological pore network model and the results for the capillary hysteresis. Section 4 discusses the lattice-Boltzmann approach and the results for the saturated permeability and the capillary hysteresis. In Section 5 the results for the different models are compared and conclusions are given. In Appendix A a detailed description of the lattice-Boltzmann model is given and in Appendix B various test cases for multiphase flows are carried out to validate the lattice-Boltzmann method.

2. Material, experimental setup and inverse parameter fit

2.1. Materials and samples

To predict the fluid distribution within the pore structure we scanned a sand sample of 1.5 cm in diameter and 1 cm in height using X-rays from a synchrotron source. The tomography was carried out at the Hamburger Synchrotron Laboratories (HASYLAB) in Germany. The particle size of the sand material ranged from 0.1 to 0.5 mm. Based on the imaged X-ray attenuation the density distribution of the solid material can be reconstructed. The reconstructed density map was segmented into a black and white image of pore space and solid phase with a voxel resolution of $r_v = 11$ μm. A voxel (*v*olumetric pi*xel*) is a volume element, representing a value on a Cartesian grid in three-dimensional space and is commonly used as the basic unit of a three-dimensional image. The tomography of this sand material is described in more detail in [22]. To avoid effects at the boundary between the sand and the container, a cube from the center of the cylinder with 800^3 voxels was analyzed with respect to geometrical properties and fluid distribution. In case of the lattice-Boltzmann approach the computation of the hysteresis in the relationship between capillary pressure and liquid saturation is very time consuming and was determined for a subcube with 200^3 voxels. The results may depend on the chosen section within the whole sample with 800^3 voxels. To estimate the sensitivity of the results on the chosen section, we focused on two subcubes with extremal properties. For that purpose, we computed characteristic geometrical properties for various subcubes. We shifted the origin of the analyzed subcube in intervals of 20 voxels in x-, y- and z-direction from position 0,0,0 to 600,600,600 within the large image. Totally, $31^3 = 29,791$

subcubes were investigated. We based the choice of the geometrical properties on the following hypothesis: (i) the fluid distribution depends on the pore volume that is quantified as porosity ϕ and (ii) on the pore size that is orthogonal to the pressure applied in z-direction that was quantified using the chord length distribution in x- and y-direction. A chord is a line entirely within the pore space between two solid particles. To determine the chord length distribution, the voxels that are arranged in a chord of length l are counted and divided by the total number of voxels of the pore space. As a characteristic length for the chord length distribution, the median of the distributions C_x and C_y in x- and y-direction were calculated. While other geometrical properties could be used to characterize the pore size as well, the chord length is the most effective to compute. For all subcubes, we computed the product $C_{geo} = \phi C_x C_y$ that has the dimension of an area. The minimum and maximum value was $113.84 r_v^2$ and $168.4 r_v^2$. The subcubes with maximum and minimum values of C_{geo} are denoted as "maximum" and "minimum" geometry and labeled as P_{Min} and P_{Max}. A subcube (also of size 200^3) from the center of the sample has the value $C_{geo} = 134.0 r_v^2$ and is labeled as P_{Med}.

2.2. Experiments and methods for parameter estimation

2.2.1. Experimental setup

The air-dry sand was packed in a 7.3 cm high column with a diameter of 9.4 cm. In order to obtain a horizontally homogeneously packed soil column, the sand was poured through a device with five consecutive sieves before it reached the column. During the filling procedure the column underneath the packing device was slowly lowered so that the distance between the device outlet and the soil surface was always ≈5 cm. The column was placed on a porous ceramic plate with a height of 0.7 cm and an absolute permeability of 1.71E−12 m². The ceramic plate in turn was in contact with a burette (Fig. 1). The experimental setup resembles the one described by [23]. A pressure transducer tensiometer was placed in the center of the column, i.e. at a height of 3.65 cm above the plate. To prevent the formation of secondary cavities during the experiment due to "escaping air bubbles", the soil surface was covered with a metal grid and weighted with approximately 1.5 kg.

During the experiment no setting or formation of additional cavities were observed. Before the Multistep-Outflow/Inflow (MSO/I) experiment was started the whole system was slowly saturated and then flushed with approximately 5 dm³ (approximately 25 times the pore volume) of degassed water from the bottom. Simultaneously the saturated permeability, K_s, was measured. To avoid evaporation at the upper boundary the column was covered with a lid. Contact to the atmosphere was assured by a thin needle. For the MSO/I experiment the pressure at the lower boundary, p_{LB}, was controlled as shown in Fig. 2. At each step the pressure changed linearly within 30 s. The one-dimensional cumulative outflow/inflow was determined by measuring the water volume in the burette, divided by the cross-section of the soil column. Cumulative outflow and the capillary pressure in the center of the column were measured with a frequency of 10 Hz and logged with a frequency of 1 Hz. At the end of the measuring procedure the sand was weighted, oven dried and again weighted to determine the water content of the column at the end and (by adding the measured cumulative outflow) the water content at the beginning of the measurement. The saturated water content, θ_s was set equal

Fig. 2. Pressure head at lower boundary of the ceramic plate, p_{LB}, for the multistep outflow/inflow experiments.

Fig. 1. Experimental setup of the multistep outflow/inflow experiments.

to the water content at the beginning. The measurements were conducted in two replications.

2.2.2. Parameter estimation by inversion of Richard's equation

The measured data was split into three branches (primary drainage, first imbibition and secondary drainage) and was thinned out, so that approximately 600 data points were left for evaluation. To obtain a maximum of information in the remaining data, the highest data density was close to the time when boundary changes occurred. The governing equation for the flow simulation was the one-dimensional Richards equation:

$$\frac{d\theta}{dp}\frac{\partial p}{\partial t} - \frac{\partial}{\partial z}\left[\frac{K(p)}{\mu}\left(\frac{\partial p}{\partial z} - \rho_w g\right)\right] = 0, \tag{1}$$

where p (Pa) is the capillary pressure, θ (–) is the volumetric water content, z (m) is the vertical length unit defined positively downward, t (s) is the time, $K(p)$ (m^2) is the absolute permeability function, μ (kg m^{-1} s^{-1}) is the dynamic viscosity and ρ_w (kg m^{-3}) and g (m s^{-2}) are the mass density of water and the acceleration due to gravity. To solve the nonlinear partial differential equation (1), appropriate initial and boundary conditions have to be specified. For our flow experiment they were chosen as follows:

$$p(0,z) = p_{LB}(0) + \rho_w g z, \quad 0 \leqslant z \leqslant L, \tag{2}$$
$$q(t,0) = 0, \quad 0 \leqslant t \leqslant t_{max}, \tag{3}$$
$$p(t,L) = p_{LB}(t), \quad 0 \leqslant t \leqslant t_{max}, \tag{4}$$

where L (m) is the column length, q (m s^{-1}) is the water flux density and t_{max} (s) is the end of the flow simulation. The constitutive relationships, i.e. the soil water retention function, $\theta(p)$, and the permeability function, $K(p)$, were described by parametric models of different flexibility. $\theta(p)$ was described by

(1) the constrained van Genuchten model [24] (vG cons):

$$S_e(p) = (1 + (\alpha|p|)^n)^{-m} \tag{5}$$

with $m = 1 - 1/n$. S_e is the water saturation, defined by

$$S_e = \frac{\theta - \theta_r}{\theta_s - \theta_r}, \tag{6}$$

where θ_r is the air entry value and α (Pa^{-1}), n (–) and m (–) are curve shape parameters.
(2) the unconstrained van Genuchten model with m as an independent fitting parameter (vG uncons)
(3) the bimodal van Genuchten model [25] (vG bimod)

$$S_e(p) = \sum_{i=1}^{2} w_i \left[\frac{1}{1 + (\alpha_i|p|,)^{n_i}}\right]^{1-\frac{1}{n_i}}, \tag{7}$$

where w_i (–) are the weighting factors for the subfunctions, subject to $0 < w_i < 1$ and $\sum w_i = 1$.
(4) and free form Hermite spline functions [26] (ff).

The permeability functions for the first 3 cases were described by the Mualem model [27]:

$$K(S_e(p)) = K_s S_e^\tau \left[\frac{\int_0^{S_e} p^{-1} dS_e^*(p)}{\int_0^1 h^{-1} dS_e^*(p)}\right]^2, \tag{8}$$

that has analytical solutions for cases 1 and 3 [28]:

$$K(p) = K_s \left[\sum_{i=1}^{k} w_i [1 + (\alpha_i|p|)^{n_i}]^{-m_i}\right]^\tau$$
$$\times \left[\frac{\sum_{i=1}^{k} w_i \alpha_i [1 - (\alpha_i|p|)^{n_i} [1 + (\alpha_i|p|)^{n_i}]^{-m_i}]}{\sum_{i=1}^{k} w_i \alpha_i}\right]^2, \tag{9}$$

where K_s is the saturated permeability and k is the modality of the function, i.e. $k = 1$ for case one and $k = 2$ for case three. For the sec-

ond case (independent m), the Mualem model was solved numerically. In the free form case $\theta(p)$ and $K(p)$ are treated as completely independent spline functions. The complexity of the models increases from case one to case four. Eq. (1) was fitted with the four different models for the constitutive relationships to the three data branches of both columns by minimizing a measure of misfit, the objective function. We obtain 24 parameter sets for $\theta(p)$ and $K(p)$ leading to a primary drainage curve (first outflow), a first imbibition curve (first inflow) and a secondary drainage curve (second outflow) for each model and soil column. The best fit parameter vector was obtained by minimizing the sum of weighted squared residuals $\Phi(\boldsymbol{b})$ between predicted and measured data, which serves as a measure of misfit,

$$\Phi(\boldsymbol{b}) = w_p \sum_{i=1}^{r_p} [p_i - \hat{p}_i(\boldsymbol{b})]^2 + w_Q \sum_{i=1}^{r_Q} [Q_i - \hat{Q}_i(\boldsymbol{b})]^2, \tag{10}$$

where $\boldsymbol{b}$ is the parameter vector, r_p and r_Q are the number of measurements for the capillary pressure and cumulative outflow and w_p and w_Q are the weighting factors for the different data types. The measured values for the capillary pressure and cumulative outflow are labeled as p_i and Q_i and the values predicted by the model as $\hat{p}_i(\boldsymbol{b})$ and $\hat{Q}_i(\boldsymbol{b})$. The values w_p and w_Q have been set to the inverse of the squared a priori assumed measurement errors σ_p and σ_Q (which were assumed to be 20 Pa and 10^{-4} m). The fitting procedure was carried out with the shuffled complex evolution algorithm [29] which is a global optimizer.

2.2.3. Saturated water content, porosity, bulk density and saturated hydraulic conductivity

The measured saturated permeability K_s was 4.09E−11/ 1.94E−11 m^2 and the saturated water content θ_s was 0.396/0.385 for column 1/2. For the imbibition branch and the secondary drainage branch θ_s was assumed to be equal to the water content at the end of the measurement (p_{LB} = +735 Pa). Here θ_s has been 0.351 for the first column and 0.343 for the second column. The bulk density ρ_b was 1567/1563 kg m^{-3} for column 1/2. The porosity ϕ was calculated with $\phi = \rho_b/\rho_s$, where ρ_s is the particle density. The particle density ρ_s was set to the density of quartz ρ_s = 2650 kg m^{-3}. The values are summarized in Tables D.1–D.3.

2.2.4. Hysteresis of the relationship between capillary pressure and saturation

The measured data and model fits for the primary drainage branch are shown in Fig. E.1. For the last two steps ($p_{LB} \leqslant -4400$ Pa) hydraulic equilibrium was not achieved. For all other steps the point water contents and capillary pressures may be predicted at any height. Although we assume a homogeneous soil without any macropores, we observed that the soil column drained already slightly at very high values for p_{LB}. This behavior can only be described by very flexible hydraulic models such as the bimodal van Genuchten model or free form approaches. The two outflow plateaus at p_{LB} = −2450 Pa in column 1 (Fig. E.1 bottom, time 3.60E+04 to 5.40E+04 s) may be explained by an instability which occurred after some fluctuations at the lower boundary. These fluctuations have no effect on the capillary pressures in the middle of the column. The resulting hydraulic property functions for the primary drainage branch (except vG uncons for clarity) are plotted in Figs. 3 and 4. The shapes of the different models look quite similar for both columns, so that we consider the experiment as well reproducible. The corresponding parameter values and goodness of fits are listed in Table D.1. Since the parameter correlation for the bimodal van Genuchten model is very high, the single parameter values should not be interpreted.

In Fig. E.2 the inflow data and corresponding fits for the first imbibition branch are shown. In column 1 hydraulic equilibrium
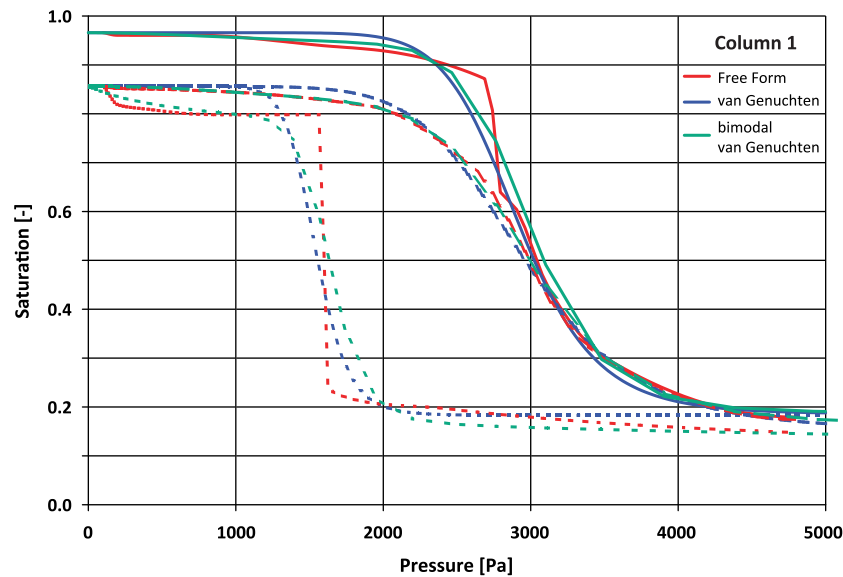
Fig. 3. Capillary hysteresis, Column 1. Solid lines: primary drainage; dots: first imbibition; dashed lines: secondary drainage.
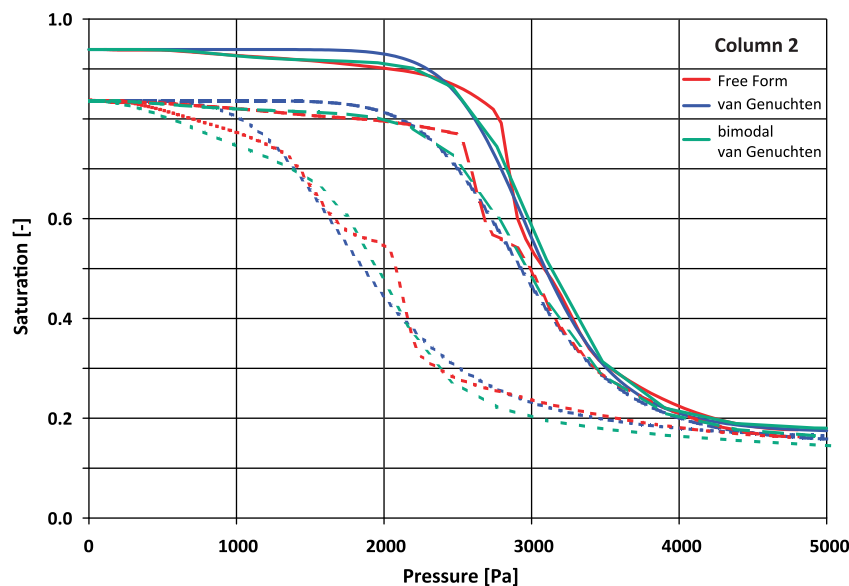

Fig. 4. Capillary hysteresis, Column 2. Solid lines: primary drainage; dots: first imbibition; dashed lines: secondary drainage.

is only reached after $p_{LB} \geqslant -980$ Pa. This late response to the change of the pressure at the lower boundary could possibly be explained by the existence of some small air bubbles underneath the ceramic plate which cause contact problems of the water phase. These air bubbles were not visible. Due to this late response almost the complete inflow happened in the last pressure steps. This can only be described by a very steep retention function close to saturation. The fit with both unimodal models failed completely. The data for column 2 looks more reasonable. But also here the system behavior can only be described adequately by the more flexible models, i.e. the bimodal or the free form approaches. The hydraulic properties functions for the first imbibition branch are shown in Figs. 3 and 4 and the corresponding parameter values are given in Table D.2. Due to the assumption that the imbibition measurement for column 1 was influenced by some measurement artifacts we suggest that the hydraulic properties functions for the imbibition branch are interpreted only from column 2.

The measured data and resulting fits for the secondary drainage branch are shown in Fig. E.3. Again, the behavior close to saturation can only adequately be described by the more flexible functions. The resulting hydraulic properties functions are plotted in Figs. 3 and 4. Again, the shapes of the different models look quite similar for both columns, so that we consider the experiment as well reproducible. The corresponding parameter values and goodness of fits are listed in Table D.3.

2.2.5. Equilibrium fit

In addition, a few equilibrium states between water saturation and capillary pressure were analyzed to validate the results of the inverse modeling. The hydraulic equilibrium data (values at the end of each pressure step until $p_{LB} = -3900$ Pa leading to 10 data points) for the four outflow branches has been fitted with the three parametric models as described in [30] with the software tool SHYPFIT2.0 (Soil Hydraulic Properties Fitting). The results are very close to the previous results and are not given here.

3. Morphological pore network model

We give a short description of the basics of the morphological pore network model. For a more detailed description we refer to [31,32]. The computation of the water retention curve with a morphological pore network model is based on a two-step procedure. Firstly, a size is assigned to each voxel of the pore space. In a second step, the replacement of a fluid phase by an invading fluid is described as an invasion percolation process. To determine the pore size, structural elements are inserted into the pore space. In case of the drainage step that is controlled by the narrowest structures, spheres with an increasing diameter are centered at each voxel of the pore space until the sphere is touching the solid phase. The radius of the sphere corresponds to the distance to the solid

phase. A voxel close to the solid is the center of a small sphere but may be an element of a larger structural element as well. In that case, the larger value is assigned to the pore voxel. The diameter of the structural element was increased in increments of two voxel sizes. For that purpose, the pore size is a multiple of the voxel size. In case of the wetting process, we tested other structural elements as well. A wetting process is affected by the widest element. For that purpose, we used two-dimensional disks as structural elements. They were inserted into planes orthogonal to the three main directions.

The replacement of the fluid phases was computed in a numerical experiment with a pressure applied at the bottom of the sample. A layer of water and air covered the bottom and top of the structure, respectively. A pore voxel was drained if the three fol-
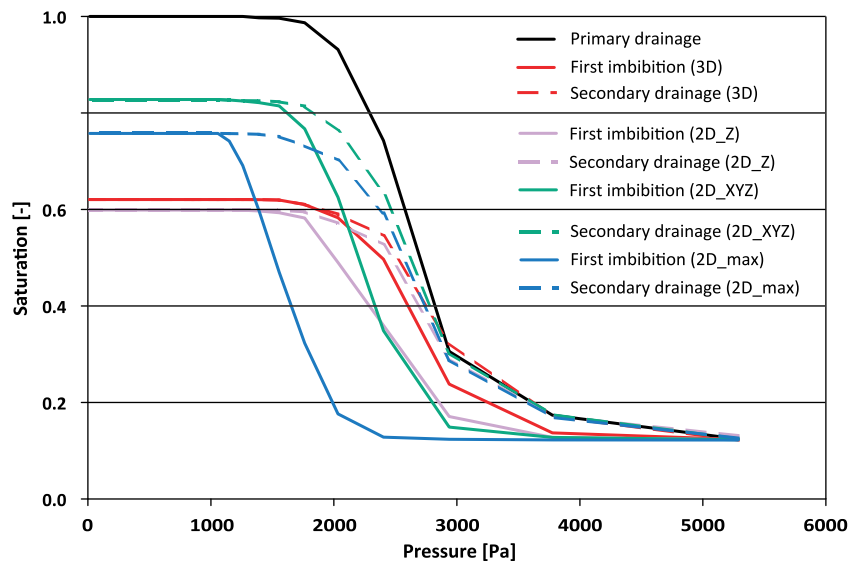
Fig. 5. The hysteresis of the relationship between capillary pressure and liquid saturation for a cube of size 200^3 voxels from the center of the total image computed with the morphological pore network model (MPN). For the computation of the wetting process, different characterizations of the pore space were applied. In one case (3D), the size of the spheres was used for the computation of the imbibition process. In all other cases, the structural elements to determine the pore size were two-dimensional. For the case "2D_Z" a disk perpendicular to the z direction was inserted. For the case "2D_XYZ", the relevant size was the disk size inserted in a plane that was orthogonal to the direction of the wetting process indicated by the position of the liquid-filled neighbor. In the last case "2D_max", the maximum disk size of all three disks perpendicular to the direction x, y and z was chosen as characteristic size. In all cases, the drainage processes were computed according to the sizes of inserted spheres.
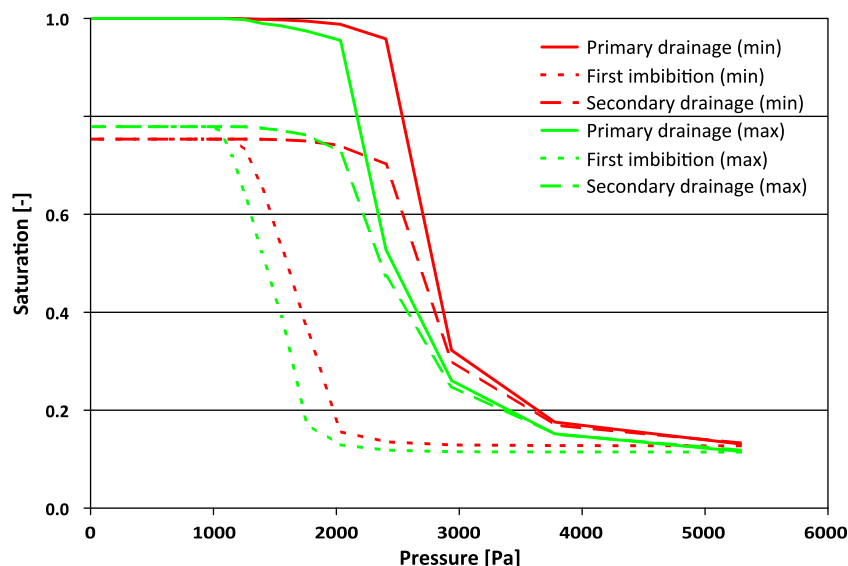
Fig. 6. The hysteresis of the water retention curve computed with MPN for two subcubes of size 200^3 voxels. For the maximum geometry, the air and water-entry values are smaller due to the larger pores.

lowing conditions are fulfilled (for the reverse wetting process, the conditions are given in parentheses):

(i) the size dependent capillary forces are smaller (larger) than the applied pressure,
(ii) the water (air) in the pore is connected to the water at the bottom (air at the top) and
(iii) air (or water) connected to the air at the top (water at the bottom) is in a neighbored pore voxel.

Initially the pore space was completely saturated with liquid. Then a pressure corresponding to the capillary forces of the largest pores in the medium was applied. The pressure was increased in intervals of $2\sigma g^{-1}\rho^{-1}(0.5dr_v)^{-1}$ with the air/water surface tension σ, the gravity acceleration g, the density of water ρ and the pore diameter dr_v with the voxel size $r_v = 11$ μm and integer values for d ranging from 1 to the maximum sphere diameter. The contact angle is assumed to be 0 and the effect of gravity is not included. We computed the primary drainage of a completely saturated pore structure and the first wetting and the secondary drainage branch of the relationship between capillary pressure and liquid saturation. In Fig. 5, the effect of the choice of the pore size relevant for the wetting process is shown. The most distinct difference between the air-entry and water-entry values (applied pressure in the wetting process to reach maximum saturation) was found for the characterization with the maximum size of the disk that can be inserted in a plane orthogonally to the x-, y- and z-direction. In addition, the maximum water saturation for the wetting process is rather small (76%) but plausible. For that purpose, the maximum size of the disk was chosen as the pore size that controls the wetting process. The hysteresis was computed for the two cubes of size 200^3 voxels with minimum and maximum $\phi C_x C_y$. The results are shown in Fig. 6. The air-entry and water-entry value are smaller for the geometry with maximum $\phi C_x C_y$ because the capillary forces are weaker in the large pores of the maximum geometry. The maximum liquid saturation for the wetting process is 75% and 78% for the minimum and maximum geometry.

4. Lattice-Boltzmann approach

4.1. Lattice-Boltzmann model, boundary conditions and grid generation

4.1.1. Lattice-Boltzmann model

The first lattice gas model for immiscible binary fluids was proposed by [33] and the equivalent lattice Bhatnagar–Gross–Krook (BGK) model was developed in [34]. Grunau [35] modified the model for binary fluids with different density and viscosity ratios on a triangular lattice in two dimensions. There are three standard LB-models for the simulation of two-phase systems: The Rothman–Keller/Gunstensen (RK) model [33–35], the Shan–Chen (SC) model [18] and the free energy (FE) approach [36]. The advantage of the RK-model is the local mass conservation of each phase and the possibility to adjust the surface tension and the ratio of densities and viscosities independently. The advantage of the Shan–Chen model is that it works with high density ratios, but the surface tension and the ratio of densities and viscosities cannot be adjusted independently. Also some parameters can only be determined by numerical experiments. The major drawback of the FE approach is the unphysical non-Galilean invariance for the viscous terms in the macroscopic Navier–Stokes equation [37]. For this work an optimized version of the Rothman–Keller/Gunstensen model developed in [1] is further modified for incompressible multiphase Stokes flow problems. A detailed description of the model is given in

Appendix A. This approach permits higher viscosity ratios and lower capillary numbers than other recent LB multiphase extensions.

4.1.2. No-slip boundary

For a single-phase flow we use the interpolation based bounce back scheme introduced in [38,39] which offers spatial second-order accuracy for arbitrarily shaped boundaries. This is especially important for the determination of permeabilities as done in Section 4.2. For multiphase flow we use the simple bounce back scheme to ensure mass conservation of all phases.

4.1.3. Inlet and outlet boundary

At the inlet and the outlet pressure boundary conditions are imposed. This is done by copying all moments given by Eq. (A.17) and the phase field values ρ_w, ρ_n from the layer next to the boundary layer itself, setting the pressure through Eq. (A.21) to the prescribed value and transforming the moments back to the distribution functions using the inverse of the transformation matrix M. For the multiphase simulations (assuming that air is the non-wetting phase and water is the wetting phase) air flow through the outlet has to be prevented. This is done by setting the velocity at the boundary layer as a function of the phase field indicator ϕ

$$v_{\text{outlet}} = \frac{1}{2}(1 + \phi)v_{\text{layer-1}}, \tag{11}$$

where $v_{\text{layer-1}}$ is the velocity next to the boundary layer. At the inlet a reservoir of non-wetting fluid is set by $\phi_{\text{inlet}} = -1$. This approach for the in- and outlet is consistent and stable.

4.1.4. Grid generation

In the literature so far, direct computations of flow through a porous medium are based on binarized porous media data mapped to uniform Cartesian grids. The tomographic voxel set is directly used as the computational grid and thus the geometrical representation is usually only first-order accurate due to staircase patterns. In this work we pursue a more elaborate approach, where the geometry is obtained as follows: Starting from a highly resolved tomographic data set we utilize a marching-cube algorithm to reconstruct all surfaces of the porous medium as a set of planar triangles. The numerical resolution of the Cartesian grid for the simulation can then be chosen independently from the voxel set. Details to this procedure can be found in [21].

4.1.5. Multiphase simulations

For two-phase flow in porous media on the microscale the important dimensionless parameters in the absence of gravity are the ratio of the dynamic viscosities and the capillary number:

$$M = \mu_n/\mu_w, \quad Ca = u_w\mu_w/\sigma, \tag{12}$$

where u_w is the wetting phase Darcy velocity, μ_n and μ_w are the dynamic viscosities of the non-wetting and the wetting phase and σ is the interfacial tension. The contact angle is set to 0 in all simulations, but other values are possible with lattice Boltzmann methods [40]. The fluid solver rescales the system in such a way that numerical errors are reduced (avoiding very small and/or large numerical values). Since this rescaling is inherent to most LB implementations, the procedure for rescaling two systems labeled as 1 and 2 with equal dimensionless parameters is presented below. The pressures between two systems 1 and 2 are related by

$$\frac{p_1 r_1}{\sigma_1} = \frac{p_2 r_2}{\sigma_2}, \tag{13}$$

where $\{r_k, k = 1,2\}$ is a reference length and the time scales are related by

$$\frac{T_1\sigma_1}{r_1\mu_1} = \frac{T_2\sigma_2}{r_2\mu_2}. \tag{14}$$

For air/water systems the ratio of $M \approx 1/50$ and the capillary number depends on the problem considered, but in most cases a low capillary number is desired. This is a challenge for numerical simulations, since there is a lower bound for the viscosity and an upper bound for the surface tension, where a stable simulation can be performed. Choosing a smaller velocity is possible, however, this leads to more time steps to be calculated and therefore to more computational effort. Also a larger ratio of M decreases the size of the time step and increases the number of time steps to be calculated. But for some problems M is insignificant for the physical process at all and for many problems ratios of $M = 1/10$ or even larger are sufficient to reproduce the main physical effects. For complex multiphase simulations the balance between parameters that yield reasonable results and numerical efficiency has to be carefully explored.

4.1.6. Simulation code and implementation

A simple lattice-Boltzmann algorithm can be implemented easily, but more advanced approaches in terms of accuracy, speed and memory consumption require careful programming. The simulation kernel called "Virtual Fluids" uses matrix based data structures and the parallelization follows a distributed memory approach using the Message Passing Interface (MPI) [41]. The kernel has been optimized with respect to speed in the first place, by e.g. using two arrays for storing the distribution functions. Collision and propagation have been combined into a single loop. The array containing the subgrid distances (q-values) is indexed by a list as they are only needed for the fluid–solid boundary nodes.

4.2. Saturated permeability of the porous medium

With the grid generation procedure described in Section 4.1.4 and the subgrid distances between the nodes of the Cartesian grid and the planar triangle surfaces we can efficiently compute permeabilities with a second-order accurate lattice-Boltzmann flow solver. Because the permeability depends strongly on the porosity of a porous medium, we investigated the dependence between the isolevel-threshold used by the marching-cube algorithm [42] to construct the triangulated surface and the resulting pore volume. We computed the reference porosity of the different subcubes P_{Min}, P_{Max} and P_{Med} defined in Section 3 (P_{Min} and P_{Max} shown in Fig. 10) just by counting the fluid (value 0) and solid cells

(value 1). The volume of the triangulated pore space was computed by using the divergence theorem. In Fig. 7 the results are shown and it turned out that the default isolevel value of 0.5 fits the reference pore volume of the voxel matrix best in all cases.

In Table 1 the permeability computed for P_{Min}, P_{Max} and P_{Med} using different grid resolutions are shown. An approximation for the permeability can be gained from the Kozeny [43] equation

$$k = \frac{m^2\phi}{5}, \tag{15}$$

where m is the ratio of the pore space volume to the wetted surface and ϕ is the porosity. Since we have a triangulated surface of the porous medium, we can easily compute the integral surface. The values are very close and indicate the high accuracy of the approximation of Kozeny. The values are not compared to the experimental results since the columns in the laboratory were not completely saturated.

4.3. P_c–S_w relationship – hysteresis

Only a few studies [44–51] have reported simulations of multiphase flow in three-dimensional porous medium systems, in part because of the computational limitations. Computations of the $S_w(P_c)$ relationship based on lattice-Boltzmann simulations can be found in [52,47,17,20]. The computations carried out for $S_w(P_c)$ relationships in [52,47] have been performed with the standard Gunstensen model. They are of qualitative nature and the grid sizes have been quite small. In [20] the grid sizes are larger, but only the primary drainage curve has been computed and compared to results from other models, but not to experimental data. Pan et al. [17] calculated the hysteresis of capillary pressure–saturation relationships using the Shan–Chen model and compared them to experimental data obtaining good results. One drawback of the method used by Pan et al. is that the primary physical parameters as the fluid–fluid and fluid–solid interaction coefficients must be deter-

Table 1
Saturated permeability, LB simulation and Kozeny's equation

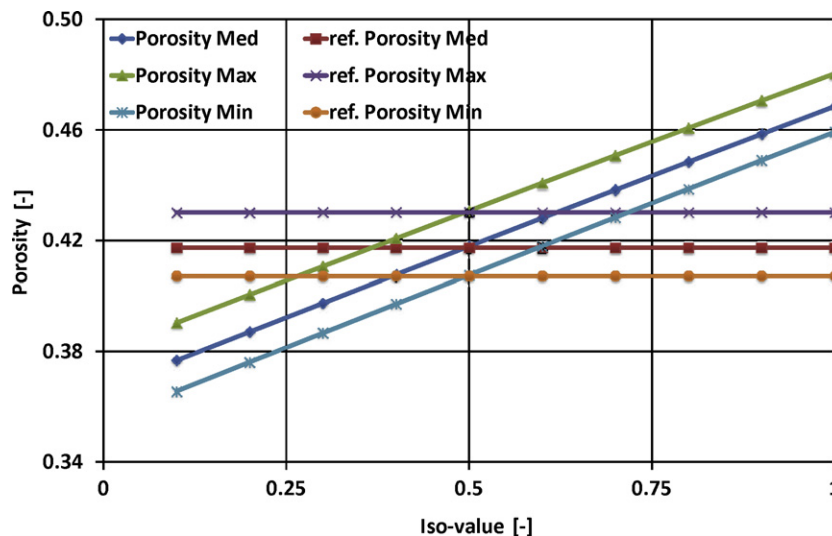| Geometry	ϕ	m	k, Eq. 15	k, LB, 151^3	k, LB, 299^3	k, LB, 399^3
P_{Min}	0.388	3.54E−5	9.74E−11	9.96E−11	9.66E−11	9.56E−11
P_{Med}	0.399	3.71E−5	1.10E−10	1.11E−10	1.07E−10	1.06E−10
P_{Max}	0.412	3.93E−5	1.28E−10	1.35E−10	1.31E−10	1.30E−10

Fig. 7. Dependence of porosity on the isolevel-threshold for three subcubes P_{Min}, P_{Max} and P_{Med}.

mined by a model calibration using numerical experiments. Also, due to a limited range of stability, the time step is very restrictive.

In our experiments we use the three subprobes P_{Min}, P_{Max} and P_{Med} for the computation of the hysteresis. In our approach we do not need a model calibration and compute the capillary pressure–saturation relationship using a system without gravity. Initially the entire pore space is filled with the wetting phase (i.e. water). To compute the $S_w(P_c)$ relationship including hysteresis a time dependent pressure difference is applied. At the top of the sample a non-wetting phase reservoir is given with a constant reference pressure $p_0 = 0$. At the bottom of the sample a time dependent decreasing pressure $p(t)$ is imposed. The static $S_w(P_c)$ relationship is a curve defined for an infinite number of pressure steps and $Ca \to 0$. In principle this could be performed by discrete pressure jumps and waiting for a steady state after each jump. But this becomes very tedious for a large number of pressure jumps, so we use a linearly increasing and decreasing pressure boundary condition to compute the primary drainage, the first imbibition and the secondary drainage:

$$p(t) = \begin{cases} -p_{max} \frac{t}{T}, & \text{if } t \in [0, T[, \\ -p_{max}\left(1 - \frac{t-T}{T}\right) & \text{if } t \in [T, 2T[, \\ -p_{max}\frac{t-2T}{T}, & \text{if } t \in [2T, 3T]. \end{cases} \quad (16)$$

The maximum pressure load p_{max} should be chosen so that the smallest pores can be evacuated and can be estimated by Eq. (B.2). To obtain a sufficiently slow process the time T has to be large. We estimate the order of the time scale by using the equation derived by Washburn [53], here modified for a linearly increasing pressure from 0 to $p = \frac{2\sigma}{r}$

$$\Delta T_{ref} = \frac{4L^2(\mu_w + \mu_n)}{\sigma r_{ref}}. \quad (17)$$

ΔT_{ref} gives an approximation for the time a two-phase system needs to penetrate a distance L into a fully wettable, porous material whose average pore radius is r_{ref}. Now we can integrate over the pore radius from r_{small} to r_{big}, where r_{small} is related to p_{max} by $p_{max} = 2\sigma/r_{small}$ and r_{big} is an approximation of the largest pore size. We obtain an estimation T_{int} for the time T in Eq. (16):

$$T_{int} = \frac{1}{\sigma} 4L^2 (\mu_w + \mu_n)(\ln r_{big} - \ln r_{small}). \quad (18)$$

To estimate T_{int}, we assume that the smallest resolvable radius is given by 2 grid spacings and the largest by approximately 20 grid spacings, we obtain $T_{int} \approx 2600 L\mu_w/\sigma$. Regarding numerical effi-

ciency, we see from Eq. (18) that for a small T_{int} a low dynamic viscosity and a high surface tension is favorable.

The dynamic dependence of the hysteresis on the time T for the sample P_{Med} is explored by choosing different times T. The parameters for the setup have been: $\mu_n = 1/200$, $\mu_w = 1/500$, $\sigma = 1/100$ and the maximum pressure was $p_{max} = \sigma/r_{ref}$, where $r_{ref} = L/200$ with L as the size of the domain. The ratio M of the dynamic viscosities is $M = 2/5$, which is far from the real world value (air/water) 1/50. This was mainly chosen to improve numerical efficiency, since for a smaller ratio the computational times have become very large. For smaller grid sizes we investigated the effect of M and found that no important effect for this type of media occurred if using larger values of M. The numerical grid size was chosen as 200^3. In Fig. 8 the results for different fast processes are shown. For simulation (A, B, C, D) we set $T = (1250, 2500, 5000, 10,000) \times L\mu_w/\sigma$ resulting in $(0.125 \times 10^6, 0.25 \times 10^6, 0.5 \times 10^6, 1.0 \times 10^6)$ LB iterations per branch. The Figures show a strong dependence of the hysteresis on T, but we see also a convergent behavior for the more saturated range of the retention curves and for the residual air saturation. For the dry range and for the residual saturation we see a strong dependence on T. For simulation D we obtain almost a residual saturation of 0 (film flow) indicating that we have a static process. The intersection of the curve in the dry range is a numerical artifact and is related to the insufficient resolution of thin films in the LB method. For subsequent simulations we use $T = T_D$ in Eq. (16).

In Fig. 9 the hysteresis for the minimum and maximum geometry P_{Min} and P_{Max} are shown. The air-entry value is higher for P_{Min} and the hysteresis is much more pronounced. The maximum liquid saturation is quite similar for both geometries and is about 0.9. In Fig. 10 the residual non-wetting phase after the imbibition for P_{Min} and P_{Max} is shown.

5. Comparison of models and results

In Figs. 11–13 the P_c–S_w relationship for the primary drainage, the first imbibition and the secondary drainage are shown. We compare the results of the curves obtained by the inversion of the Richards equation (see Section 2.2.2), by the morphological pore network model (see Section 3 and Fig. 6) and the lattice-Boltzmann model (see Section 4.3). The geometry P_{Med} for the morphological pore network model (MPN) and lattice-Boltzmann model (LB) was a cube of the size 200^3 from the center of the sample (see Section 2.1).
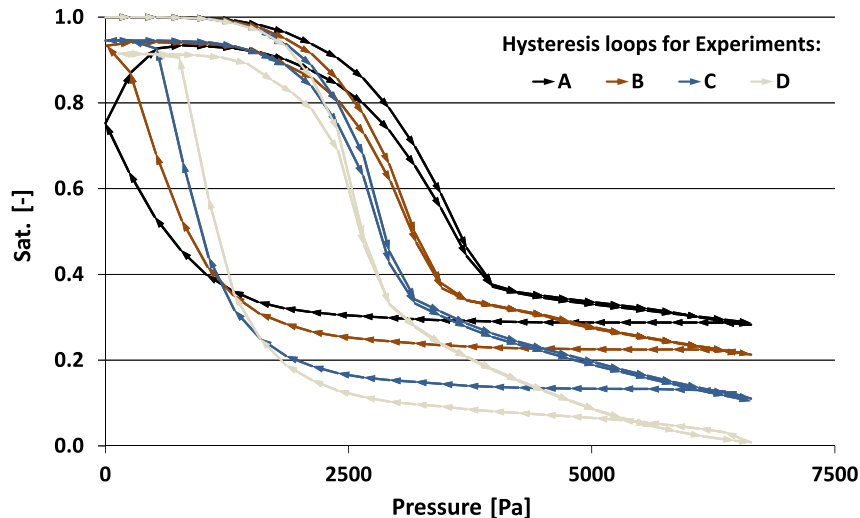

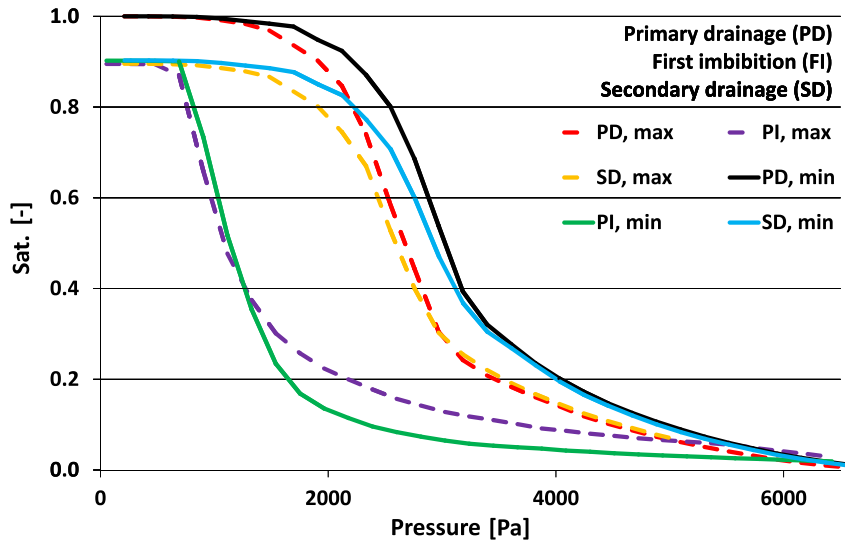**Fig. 8.** LB Simulation (P_{Med}) of hysteresis by different fast processes.

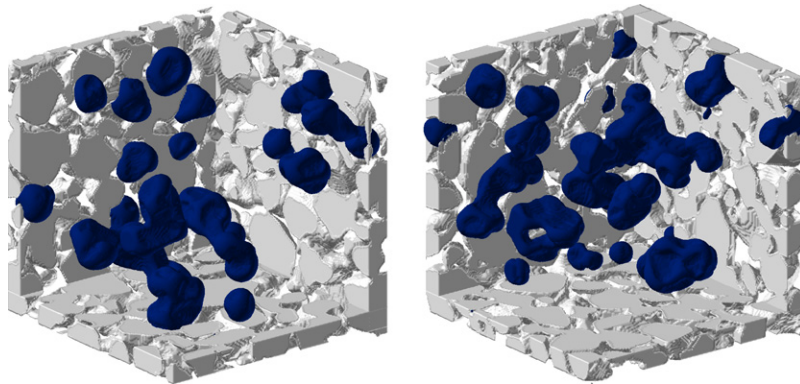**Fig. 9.** LB simulations of hysteresis for different geometries (P_{Min} and P_{Max}).

Fig. 10. Residual air saturation after the imbibition, left: maximum geometry P_{Max}, right: minimum geometry P_{Min}.
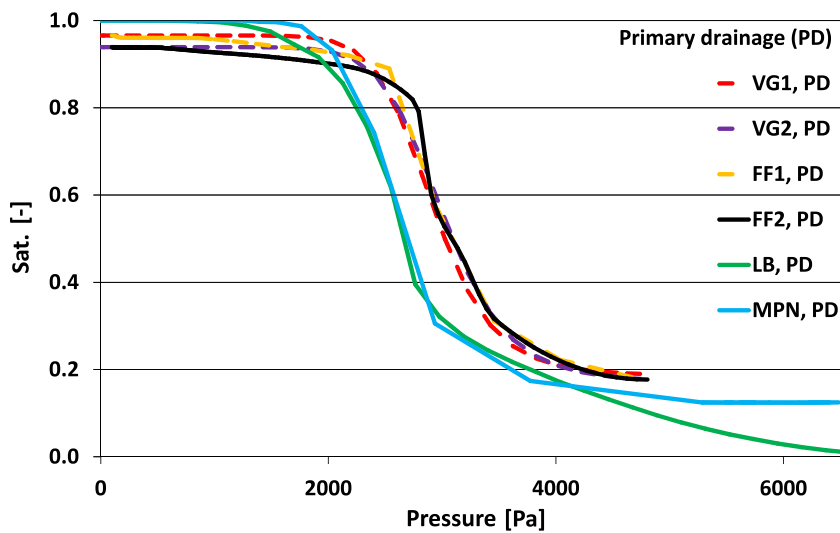

Fig. 11. Primary drainage (PD): morphological pore network model, LB simulation and parameter fits VG and FF.

For the primary drainage the results of the LB simulation and the morphological pore network model show a very good agreement. Only in the dry range, where the LB model suffers from the problem of thin-film flow discussed in Section B.5 and resolution problems of the wetting phase discussed in Section B.1, we noticed deviations. The results of the inverse fit (VG = Van Genuchten
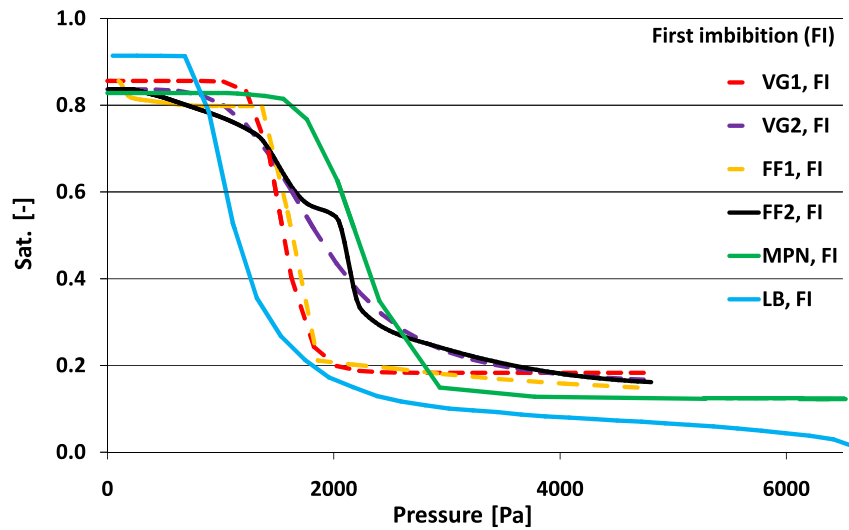
Fig. 12. First imbibition (FI): morphological pore network model, LB simulation and parameter fits VG and FF.
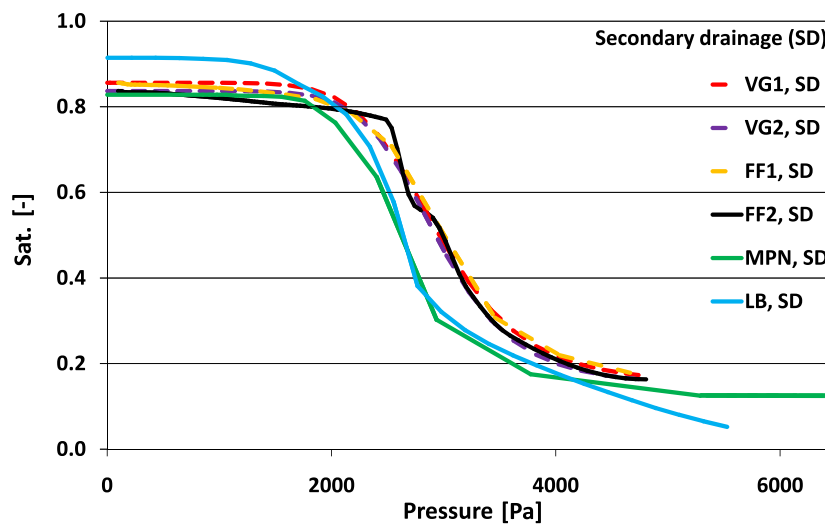
Fig. 13. Secondary drainage (SD): morphological pore network model, LB simulation and parameter fits VG and FF.
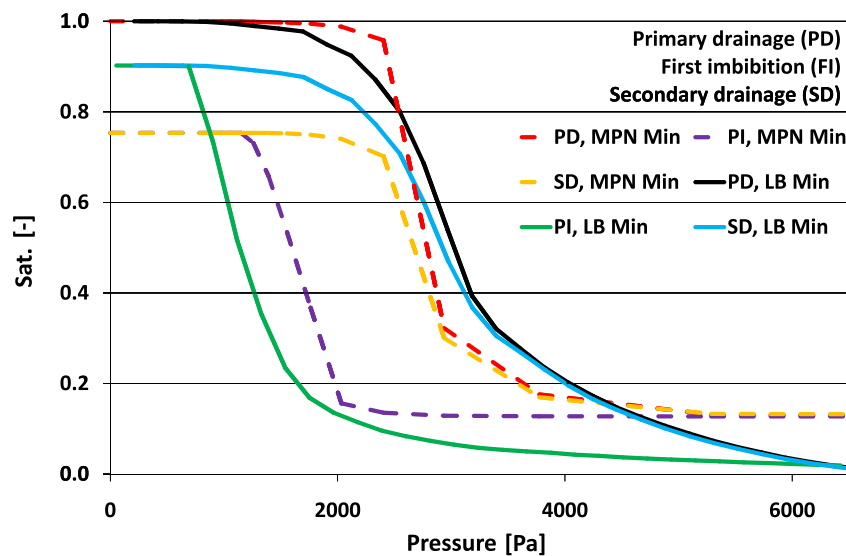
Fig. 14. Minimum geometry, LB and MPN results.

constrained, FF = free form) from column 1 and 2 are very similar. They deviate from the results of the LB and MPN methods in amplitude by approximately 10%. The value of the slope agrees very well. The residual saturation predicted by the MPN model is 12% and the inverse fit predicts values from 15% to 18%.

For the first imbibition the results by the inverse fit (VG = Van Genuchten constrained, FF = free form) from column 1 and 2 differ. For column 1 we had a very late response leading to a step function for the data FF1 shown in Fig. 12, but the van Genuchten fit smoothes out this behavior. The results for column 2 are smoother. Nevertheless the results obtained by either the LB or the MPN approach show more resemblance to the results from column 1. In the saturation range between 0.2 and 0.7 the LB and MPN results have a similar slope but the amplitude of the latter is 25% higher. The maximum water content for the wetting process is 84–86% for the experimental, 76% for the MPN and 90% for the LB results.

For the secondary drainage the results from the LB simulation and the MPN model show a very good agreement in the range of saturations between 0.6 and 0.15. In the wetter range the difference is due to the different residual air saturations from the first imbibition. In the dry range the LB method drains almost completely due to film flow. The results for the inverse fit (VG = Van Genuchten constrained, FF = free form) from column 1 and 2 are very similar. They deviate from the results of LB and MPN model in amplitude by approximately 10%. Again the value of the slope agrees very well.

In Fig. 14 the hysteresis for the minimum geometry, in Fig. 15 the hysteresis for the maximum geometry, obtained from the LB simulation and MPN method are shown. They show good agreement for the drainage curves, yet for the imbibition the deviations are larger. The air-entry pressure for the minimum geometry is higher than for the maximum geometry and this behavior is reproduced by both models. This can be explained by the smaller throats of the pore space in the minimum geometry (small pore width and porosity) that need a higher pressure to be drained. The maximum water content for the wetting process is approximately 0.9 in both cases for LB and 0.75 (minimum geometry) and 0.78 (maximum geometry) for the morphological pore network model. Referring to the LB results, the hysteretic effect is much more pronounced for the minimum than for the maximum geometry. We observe the same behavior in weaker form for the MPN model as well.

6. Conclusions and outlook

We evaluated the capability of two different multiphase models to predict the hysteretic behavior of the capillary pressure saturation relationship on the basis of detailed representations of the complex porous structure as measured by X-ray tomography. The models differ considerably in complexity and computational costs and can have different potential applications. However, the results obtained for the primary and secondary drainage curve are consistent, while differences among the models for the first imbibition are observed.

In general MPN models are sufficient to compute the primary drainage, but the choice of the structural element for imbibition is not straightforward and changes the results considerably. In contrast the LB approach needs no modeling (no structural element) for the imbibition, but due to a lack of resolution in the dry range, numerical errors become large and reliable results are difficult to obtain.

Our work permits the following conclusions:

- The air-entry pressure and the slope of the drainage curves can be predicted by the LB- and the MPN model very well.
- With the morphological pore network model the residual water saturation can be predicted, for the LB approach this task is more difficult due to the limited resolution thin-film flow. In Section B.5 a method using the LB approach for the prediction of the residual saturation in a sphere packing is investigated.
- The residual air saturation can be predicted by both models. The LB model predicts a smaller amount of residual air than the morphological pore network model. The experimental results are in between.
- In the case of the morphological pore network model, the results depend on the choice of the structural elements to quantify the pore space. While the choice of spheres is reasonable for a drainage process limited by the smallest curvature radius, the choice for the wetting process is not straightforward.
- The standard LB approach using uniform grids is limited in the dry range. This is due to the insufficient resolution of thin water films and thus leads to erroneous capillary pressures. One possible solution for the dry range is to use a non-uniform, adaptive LB approach. Methods for simulations of two-phase flows using non-uniform grids have been developed in [1]. Using grid refinement for two-phase flow in porous media is a challenge.
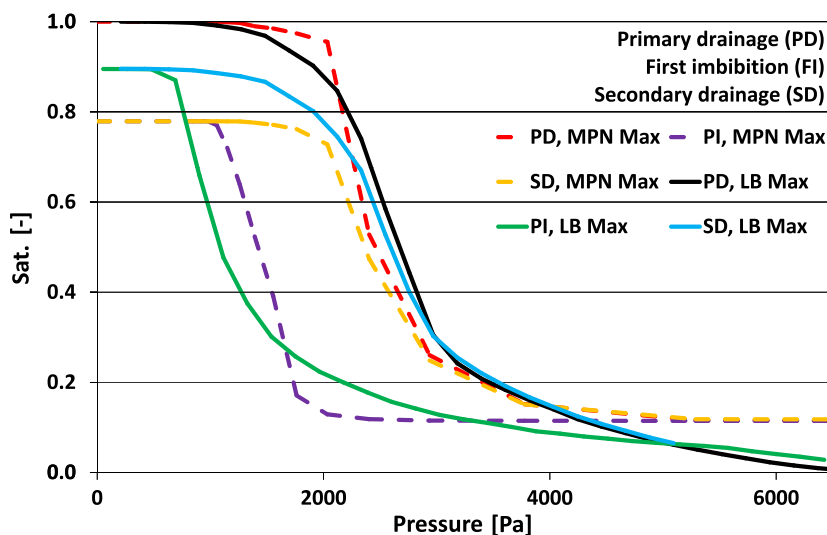

Fig. 15. Maximum geometry, LB and MPN results.

- Only with the LB approach it is possible to simulate a fully resolved simulation of dynamic multiphase phenomena tracking the interface evolution. Except for the limitation mentioned before, the consistency of the results indicates a reliable representation of the multiphase dynamics.
- The computational costs of LB simulations are orders of magnitudes higher than for the MPN model, so it is difficult to do a sound statistics covering a lot of different geometries with the present computational resources.
- Dynamic pore network models can also simulate dynamic phenomena, but here some simplifications and assumptions have to be made which introduce potential modeling errors. For an advanced network model we refer to [54,55]. One difficulty is to map the pore space to an equivalent pore network representation [16]. On the other hand, the insufficient numerical resolution of the thin-film flow in the LB model in the dry range leads to numerical errors.
- Comparing to the work of [17] on simulation of hysteresis we can observe the following common behavior: The amplitude of the drainage is approx. 10% below the experimental values and the irreducible air saturation is higher than the experimental values. In contrast the amplitude of the first imbibition in our simulation is below the experimental values, whereas in [17] it is above.

Acknowledgements

Appendix A. Multiphase lattice-Boltzmann model

The lattice-Boltzmann method is a numerical method to solve the Navier–Stokes equations [56–58], where density distributions propagate and collide on a regular lattice. A common labeling for different lattice-Boltzmann models is $dxqb$ [59], where x is the space dimension and b the number of microscopic velocities. We use a three-dimensional nineteen velocity lattice-Boltzmann model (d3q19) for immiscible binary fluids described in [1], which allows adjusting the surface tension and the ratio of viscosities independently. Here we give a short review of the model optimized for Stokes flow. In the following discussion the font bold sans serif ($\mathbf{x}$) represents a three-dimensional vector in space and the font bold with serif $\boldsymbol{f}$ a b-dimensional vector, where b is the number of microscopic velocities. The microscopic velocities are given with

A.1. Lattice-Boltzmann method for the phase field

We introduce a wetting and non-wetting dimensionless density field ρ_{w} and ρ_{n} and define an order parameter ϕ

$$\phi = \frac{\rho_{\mathrm{w}} - \rho_{\mathrm{n}}}{\rho_{\mathrm{w}} + \rho_{\mathrm{n}}}, \tag{A.1}$$

which indicates the fluid phase: $\phi = 1$ for the wetting phase and $\phi = -1$ for the non-wetting phase. The value of ϕ is constant in the bulk of each phase and varies only in the diffusive fluid–fluid interface.

The gradient $\mathbf{C}$ of ϕ is computed by

$$\mathbf{C}(t, \mathbf{x}) = \frac{3}{c^2 \Delta t} \sum_i w_i \mathbf{e}_i \phi(t, \mathbf{x} + \mathbf{e}_i \Delta t). \tag{A.2}$$

The normalized gradient is

$$n_\alpha = \frac{C_\alpha}{|\mathbf{C}|} \tag{A.3}$$

and defines the orientation of the fluid–fluid interface.

The advection of the density fields $\psi = \{\rho_{\mathrm{w}}, \rho_{\mathrm{n}}\}$ is done with the following LB equation:

$$g_i(t + \Delta t, \mathbf{x} + \mathbf{e}_i \Delta t) = g_i^{\mathrm{eq}}(\psi(t, \mathbf{x}), \mathbf{u}(t, \mathbf{x})), \tag{A.4}$$

where g_i are dimensionless density distributions. The equilibrium distribution function g_i^{eq} is given by

$$g_i^{\mathrm{eq}}(\psi, \mathbf{u}) = w_i \psi \left(1 + \frac{3}{c^2} \mathbf{e}_i \cdot \mathbf{u}\right). \tag{A.5}$$

The velocity $\mathbf{u}$ is computed by the flow solver described in Section A.2. The weights w_i are

$$w_i = \begin{cases} \frac{1}{3} & \text{for } i = 0, \\ \frac{1}{18} & \text{for } i = 1, 2, 3, 4, 5, 6, \\ \frac{1}{36} & \text{for } i = 7, 8, 9, 10, 11, 12, 13, 14, 15, 16, 17, 18. \end{cases} \tag{A.6}$$

The scheme (A.4) in combination with (A.5) results in an advection diffusion equation [60]. The diffusion coefficient is $\alpha = \frac{1}{6} c^2 \Delta t$ which is annihilated by the following algorithm: A recoloring step is introduced to eliminate the diffusion effects and to achieve a phase separation. The recoloring step redistributes the distributions g_i of phase ρ_{r} and ρ_{b} so that the inner product of the gradient $\mathbf{C}$ and the momentum of phase ρ_{r} is maximized. The constraints are the conservation of the mass of each phase and the conservation of the momentum of the sum of both phases. We use the recoloring algorithm given in [47,40].

Note that for the scheme given by (A.4) we only need the value ψ of the phase field and the advection velocity $\mathbf{u}$ as input values. So

$$\{\mathbf{e}_i, i = 0, \ldots, 18\} = \begin{Bmatrix} 0 & c & -c & 0 & 0 & 0 & 0 & c & -c & c & -c & c & -c & c & -c & 0 & 0 & 0 & 0 \\ 0 & 0 & 0 & c & -c & 0 & 0 & c & -c & -c & c & 0 & 0 & 0 & 0 & c & -c & c & -c \\ 0 & 0 & 0 & 0 & 0 & c & -c & 0 & 0 & 0 & 0 & c & -c & -c & c & c & -c & -c & c \end{Bmatrix},$$

where c is a constant microscopic reference velocity. The microscopic velocities define a space-filling computational lattice where a node is connected to the neighboring nodes through the vectors $\{\Delta t \mathbf{e}_i, i = 0, \ldots, 18\}$. The time step Δt defines the grid spacing through $h = c\Delta t$. We use two LB schemes: The scheme described in Section A.1 is used for the advection of two-phase fields indicating the different fluid phases. The scheme described in Section A.2 is the flow solver including the effects of surface tension.

we need to store only the two variables ρ_{r} and ρ_{b} and not the corresponding nineteen distribution functions for each field.

A.2. Generalized lattice-Boltzmann method for the flow field

We use the generalized lattice-Boltzmann (GLB) equation introduced in [61,62] in a modified version [1] and give here a description optimized for Stokes flow.

The lattice-Boltzmann equation is given by

$$f_i(t + \Delta t, \mathbf{x} + \mathbf{e}_i \Delta t) = f_i(t, \mathbf{x}) + \Omega_i, \quad i = 0, \dots, b - 1, \tag{A.7}$$

where f_i are mass fractions (unit kg m^{-3}) propagating with velocities $\mathbf{e}_i$. The collision operator of the multi-relaxation time model (MRT) is given by

$$\Omega = \mathsf{M}^{-1}\mathsf{S}((\mathsf{M}f) - m^{\mathrm{eq}}). \tag{A.8}$$

The transformation matrix M

$$M_{i,j} = \Phi_{i,j}, \quad i, j = 0, \dots, b - 1 \tag{A.9}$$

is constructed from the orthogonal basis vectors $\{\boldsymbol{\Phi}_i, i = 0, \dots, b - 1\}$

$$\Phi_{0,\alpha} = 1, \quad \Phi_{1,\alpha} = \mathbf{e}_\alpha^2 - c^2, \quad \Phi_{2,\alpha} = 3(\mathbf{e}_\alpha^2)^2 - 6\mathbf{e}_\alpha^2 c^2 + c^4, \tag{A.10}$$

$$\Phi_{3,\alpha} = e_{\alpha x}, \quad \Phi_{5,\alpha} = e_{\alpha y}, \quad \Phi_{7,\alpha} = e_{\alpha z}, \tag{A.11}$$

$$\Phi_{4,\alpha} = (3\mathbf{e}_\alpha^2 - 5c^2)e_{\alpha x}, \quad \Phi_{6,\alpha} = (3\mathbf{e}_\alpha^2 - 5c^2)e_{\alpha y}, $$

$$\Phi_{8,\alpha} = (3\mathbf{e}_\alpha^2 - 5c^2)e_{\alpha z}, \tag{A.12}$$

$$\Phi_{9,\alpha} = 3e_{\alpha x}^2 - \mathbf{e}_\alpha^2, \quad \Phi_{11,\alpha} = e_{\alpha y}^2 - e_{\alpha z}^2, \tag{A.13}$$

$$\Phi_{13,\alpha} = e_{\alpha x}e_{\alpha y}, \quad \Phi_{14,\alpha} = e_{\alpha y}e_{\alpha z}, \quad \Phi_{15,\alpha} = e_{\alpha x}e_{\alpha z}, \tag{A.14}$$

$$\Phi_{10,\alpha} = (2\mathbf{e}_\alpha^2 - 3c^2)(3e_{\alpha x}^2 - \mathbf{e}_\alpha^2), \quad \Phi_{12,\alpha} = (2\mathbf{e}_\alpha^2 - 3c^2)(e_{\alpha y}^2 - e_{\alpha z}^2), \tag{A.15}$$

$$\Phi_{16,\alpha} = (e_{\alpha y}^2 - e_{\alpha z}^2)e_{\alpha x}, \quad \Phi_{17,\alpha} = (e_{\alpha z}^2 - e_{\alpha x}^2)e_{\alpha y}, $$

$$\Phi_{18,\alpha} = (e_{\alpha x}^2 - e_{\alpha y}^2)e_{\alpha z} \tag{A.16}$$

and transforms the distributions into moment space. In Appendix C the matrix is given in full detail. The resulting moments $\boldsymbol{m} = \mathsf{M}f$ are labeled as

$$m = (\delta\rho, e, \xi, \rho_0 u_x, q_x, \rho_0 u_y, q_y, \rho_0 u_z, q_z, p_{xx}, \pi_{xx}, p_{ww}, \pi_{ww}, p_{xy}, p_{yz}, p_{xz},$$
$$m_x, m_y, m_z), \tag{A.17}$$

where $\delta\rho$ is a density variation, $\mathbf{j} = \rho_0 (u_x, u_y, u_z)$ is the momentum, ρ_0 is a constant reference density and $\mathbf{u} = (u_x, u_y, u_z)$ is the velocity vector. The moments $e, p_{xx}, p_{ww}, p_{xy}, p_{yz}, p_{xz}$ of second order are related to the strain rate tensor. The other moments of higher order are related to higher order derivatives of the flow field and have no direct physical impact with respect to the incompressible Navier–Stokes equations.

The vector $\boldsymbol{m}^{\mathrm{eq}}$ is composed of the equilibrium moments extended by terms responsible for the generation of surface tension and is given by

$$m_0^{\mathrm{eq}} = \delta\rho, \tag{A.18a}$$

$$m_1^{\mathrm{eq}} = e^{\mathrm{eq}} = -\sigma \mid \mathbf{C} \mid, \tag{A.18b}$$

$$m_3^{\mathrm{eq}} = \rho_0 u_x, \tag{A.18c}$$

$$m_5^{\mathrm{eq}} = \rho_0 u_y, \tag{A.18d}$$

$$m_7^{\mathrm{eq}} = \rho_0 u_z, \tag{A.18e}$$

$$m_9^{\mathrm{eq}} = 3p_{xx}^{\mathrm{eq}} = \frac{1}{2}\sigma \mid \mathbf{C} \mid (2n_x^2 - n_y^2 - n_z^2), \tag{A.18f}$$

$$m_{11}^{\mathrm{eq}} = p_{zz}^{\mathrm{eq}} = \frac{1}{2}\sigma \mid \mathbf{C} \mid (n_y^2 - n_z^2), \tag{A.18g}$$

$$m_{13}^{\mathrm{eq}} = p_{xy}^{\mathrm{eq}} = \frac{1}{2}\sigma \mid \mathbf{C} \mid (n_x n_y), \tag{A.18h}$$

$$m_{14}^{\mathrm{eq}} = p_{yz}^{\mathrm{eq}} = \frac{1}{2}\sigma \mid \mathbf{C} \mid (n_y n_z), \tag{A.18i}$$

$$m_{15}^{\mathrm{eq}} = p_{xz}^{\mathrm{eq}} = \frac{1}{2}\sigma \mid \mathbf{C} \mid (n_x n_z), \tag{A.18j}$$

$$m_2^{\mathrm{eq}} = m_4^{\mathrm{eq}} = m_6^{\mathrm{eq}} = m_8^{\mathrm{eq}} = m_{16}^{\mathrm{eq}} = m_{17}^{\mathrm{eq}} = m_{18}^{\mathrm{eq}} = 0. \tag{A.18k}$$

The definitions of $\mathbf{C}$ and $\mathbf{n}$ are given in Eqs. (A.2) and (A.3).

The moments $\{m_k, k = 0, 3, 5, 7\}$ are conserved during the collision, leading to mass and momentum conservation of the algorithm. The matrix S is a diagonal collision matrix composed of relaxation rates $\{s_{i,i}, i = 1, \dots, b-1\}$, also called the eigenvalues of the collision matrix $\mathsf{M}^{-1}\mathsf{SM}$. The rates which are different from zero are

$$s_{1,1} = -s_e,$$
$$s_{2,2} = -s_\xi,$$
$$s_{4,4} = s_{6,6} = s_{8,8} = -s_q,$$
$$s_{10,10} = s_{12,12} = -s_\pi,$$
$$s_{9,9} = s_{11,11} = s_{13,13} = s_{14,14} = s_{15,15} = -s_v,$$
$$s_{16,16} = s_{17,17} = s_{18,18} = -s_m.$$

The relaxation rate s_v is related to the kinematic viscosity v by

$$\frac{1}{s_v} = 3\frac{v}{c^2 \Delta t} + \frac{1}{2}. \tag{A.19}$$

The other relaxation rates s_e, s_ξ, s_q, s_π and s_m can be freely chosen in the range $[0, 2]$ and may be tuned to improve accuracy and/or stability [62]. The optimal values depend on the specific system under consideration (geometry, initial and boundary conditions) and cannot be computed in advance for general cases. For Stokes flow a good choice are the "magic" parameters relaxing the even and the odd moments differently [63]:

$$s_e = s_\xi = s_\pi = s_v, s_q = s_m = 8\frac{(2 - s_v)}{(8 - s_v)}. \tag{A.20}$$

The pressure variation δp is given by

$$\delta p = \frac{c^2}{3}\delta\rho. \tag{A.21}$$

A detailed mathematical analysis shows that this numerical model yields the Navier–Stokes equation for two immiscible phases with surface tension [60] (for single-phase flow see [56,64]). The scheme is formally first order in time and second order in space. Note that the extensions to the original method [34], especially the linear advection scheme, the moment method and the altered terms (A.18b)–(A.18k) for imposing surface tension, substantially improve the numerical efficiency. A method for adjusting the contact angle between the wetting and non-wetting phase is proposed in [40].

Appendix B. Validation of the lattice-Boltzmann model

Different validation examples have been set up to test and explore the LB method proposed here for the simulation of multiphase flow problems in porous media.
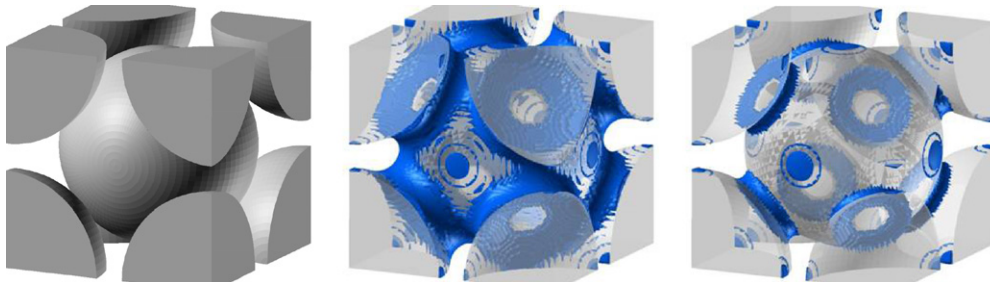

Fig. B.1. Pendular rings between solids at different saturations in a BCC array of spheres. Left: plain geometry, middle and right: computational results.

B.1. Pendular rings

Schubert [65] computed the shape using the Laplace equation of fluid bridges between spheres neglecting gravity and tabulated relations for the capillary pressure and the saturation in sphere packings assuming that the wetting phase is distributed as pendular rings [65, see p. 128, Fig. 4.12; p. 138, Fig. 4.24]. The values can be recovered from the tables with an accuracy of approximately 5%. As a test case we use a body centered cubic (BCC) array of spheres shown in Fig. B.1 with a porosity of 0.32. Periodic boundary conditions for all directions are imposed and the wetting phase is pre-initialized in such a way that pendular rings result as a static solution. The capillary pressure is computed by averaging the pressures in both phases and computing the difference. The parameters for the simulation have been chosen as follows: The grid resolution is 96^3, the viscosities are $\mu_w = \frac{1}{60}$ Pa s, $\mu_n = \frac{1}{600}$ Pa s and the interfacial tension is $\sigma = 0.01$ N m^{-1}. These values are close to the values we used for the simulations in a natural porous media carried out in Section 4.3. The results are shown in Fig. B.2, where the saturation against the dimensionless capillary pressure $p_c d/\sigma$ (d is the diameter of the sphere) is shown. In the case of low saturations the wetting phase is only resolved by a few grid points, so that due to insufficient numerical resolution the resulting capillary pressure deviates more from the results given in [65]. In Fig. B.1 the resulting shape for two configurations are shown.
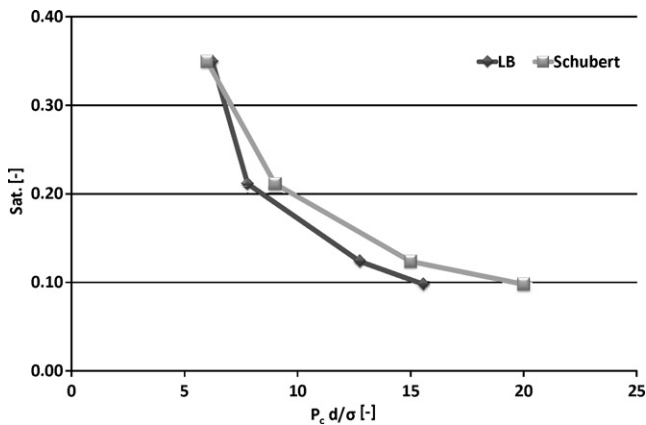
B.2. Static capillary tube bundle

As a test case the capillary pressure saturation relationship for a bundle of capillary tubes is computed by a numerical simulation. The layout of the tube bundle is shown in Fig. B.3. The radii differ by one order of magnitude; the diameter of the smallest tube is resolved by approximately four grid points, the largest by approximately 20 grid points. The overall system is resolved by 124×108 grid points in the cross-section and 100 grid points along the tubes. The viscosities are $\mu_w = \frac{1}{60}$ Pa s, $\mu_n = \frac{1}{600}$ Pa s and the interfacial tension is $\sigma = 0.01$ N m^{-1}. The system has been initialized with different saturations where the wetting phase was distributed at a certain fill level uniformly over the different tubes. The tubes are connected at the top to the non-wetting phase reservoir and at the bottom they are interconnected by a small layer of two grid spacings perpendicular to the tubes. Thus the system is allowed to equilibrate itself, so that the largest tubes are evacuated and the smaller ones are filled. After reaching a steady state the pressure is measured in the wetting phase. The theoretical solution is piecewise constant and compared to the

Fig. B.2. Capillary pressure for pendular rings at different saturations.
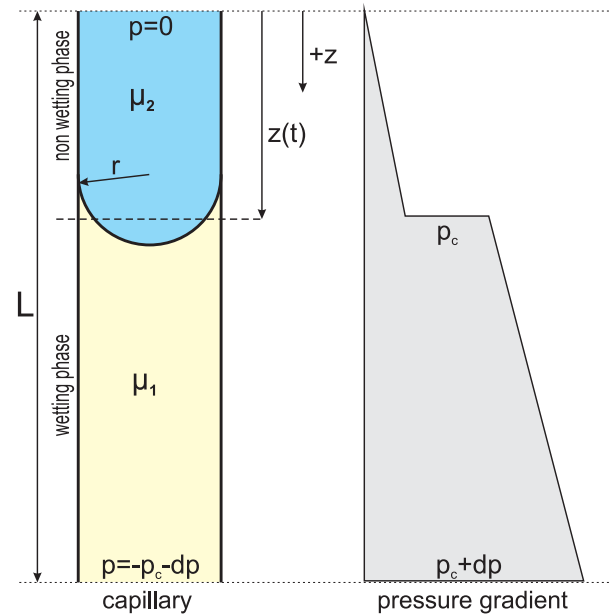
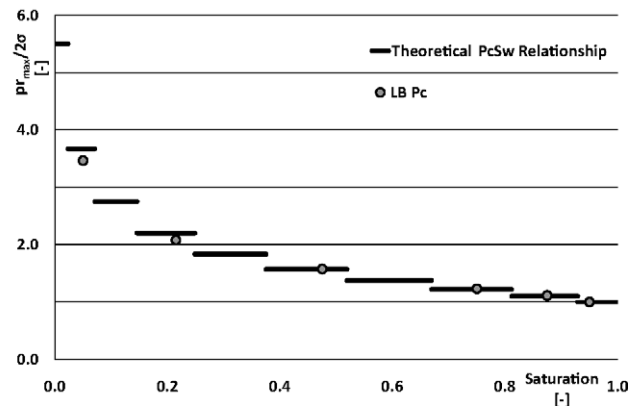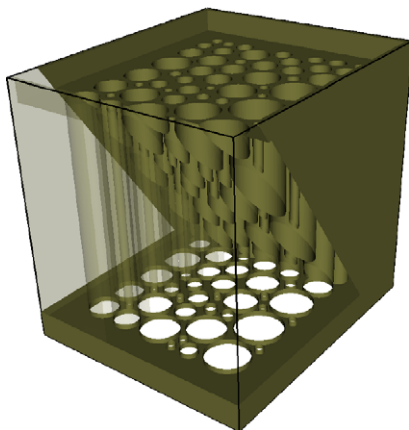

Fig. B.4. Definitions for the Washburn equation.

Fig. B.3. Left: static capillary tube bundle, right: capillary pressure – saturation relationship for a capillary tube bundle.
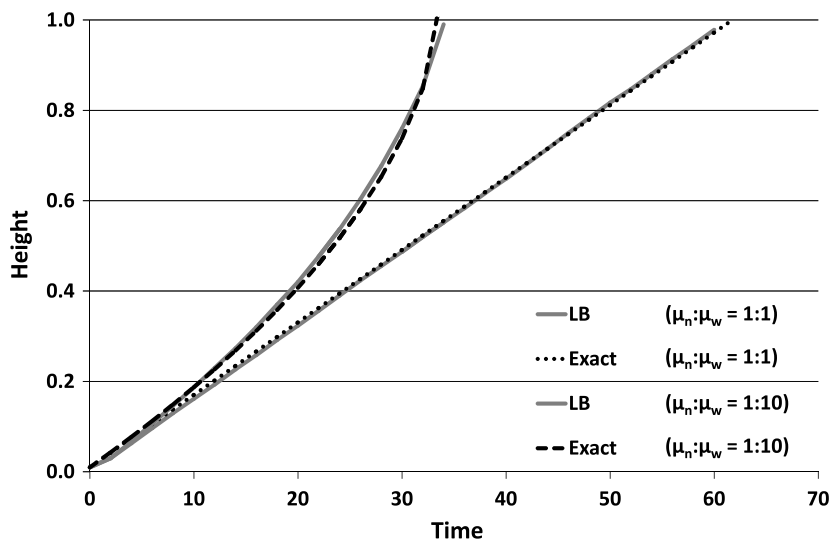
Fig. B.5. Results from the numerical capillary rise experiment.

results of the simulations represented by dots in Fig. B.3. The pressure is normalized with respect to the entry pressure $2\sigma/r_{max}$. In the case of low saturations the wetting phase is only resolved by a few grid points, so that due to insufficient resolution the resulting capillary pressure deviates more from the analytical results.

B.3. Capillary rise

The rise of a single capillary tube as shown in Fig. B.4, driven by a pressure difference dp at the top and the bottom can be computed by the Washburn solution [53] in the absence of gravity according to
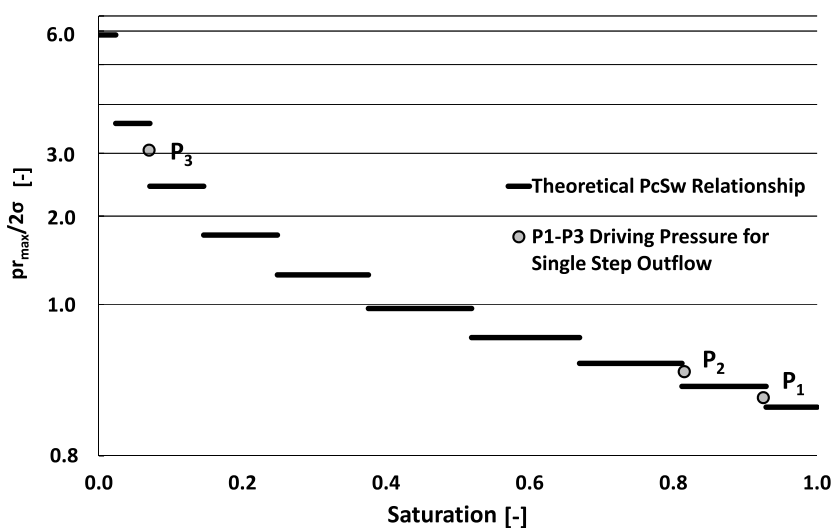

Fig. B.6. Three different pressure loads for the tube bundle (single step outflow).
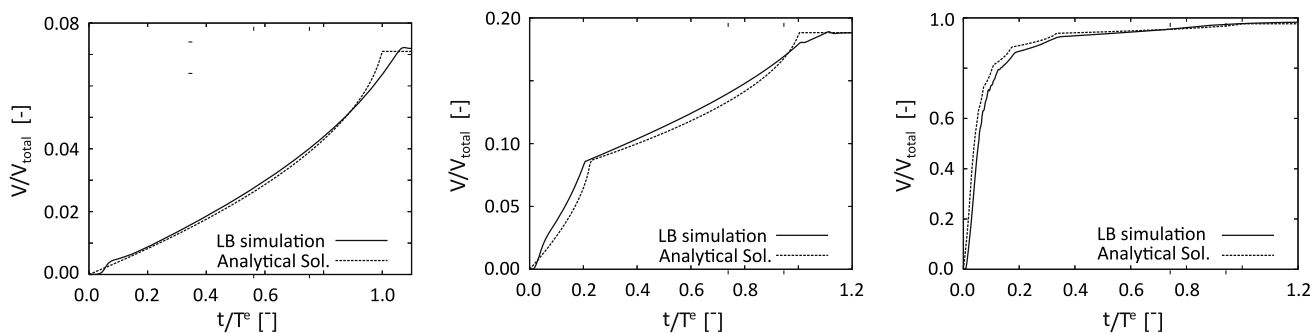

Fig. B.7. Results for different pressure loads for the capillary tube bundle.

$$z(t) = \frac{1}{\mu_w - \mu_n}\left(\mu_w L - \sqrt{\left(L^2\mu_w^2 + \frac{dpr^2}{4}(\mu_n - \mu_w)t\right)}\right). \tag{B.1}$$

For the simulation the ratio of the length L and the radius r is $L/r = 20$. We have performed simulations with two different setups: in the first simulation both phases had the same viscosity $\mu_w = \mu_n = 1/6$ Pa s, in the second simulation the ratio of viscosities has been set to 10, $\mu_w = 1/6$ Pa s, $\mu_n = 1/60$ Pa s. The surface tension was set to 0.01 N m^{-1} and the driving pressure was $dp = 1.30\ p_c$, where $p_c = 2\sigma/r$. In Fig. B.5 the results for both cases are given where the height is height $= z(t)/L$ and on the x-axis the dimensionless time $T\sigma/(L\mu_w)$ is given.

B.4. Dynamics of a capillary tube bundle

The tube bundle setup discussed in Section B.2 has been used for different single step outflow experiments. The grid resolution and the material parameters are the same as in Section B.2. Three different simulations with different pressure loads P1, P2, P3 shown in Fig. B.6 have been performed. The analytical solution of the outflow of the wetting phase can be computed by integrating the Washburn solution (B.1)

$$V(t) = \pi\sum_{k=1}^{M} N_k r_k^2 (L - z_k(t)),$$

where M is the number of different classes of tubes, N_k is the number of tubes within one class, r_k is the radius and $z_k(t)$ is the Washburn solution B.1. In Fig. B.7 the results from the simulation and the analytical solution are given for the three different test cases. The time scale has been normalized with respect to the time T_e, where the analytic solution does not change anymore. Besides minor deviations at the start and end of the drainage process, where the assumption for the Washburn equation are only approximately fulfilled, the agreement is good.

B.5. Residual water saturation for a porous medium

Due to the phase field approach in the lattice-Boltzmann method for multiphase flow, a diffusive interface of approximately three lattice spacings between the fluid phases exists. If we drain a porous medium initially filled with wetting phase, we are left with a very thin layer of wetting phase covering the matrix, meaning that the value of the order parameter ϕ (A.1) in drained cells next to the walls are close to the value of the non-wetting phase, but never drain completely. Due to this effect we obtain a hydraulically conducting thin film. Consequently we can drain each geometrically connected porous medium almost completely if we apply a pressure which is in the range of the maximal capillary pressure B.2 due to the grid resolution. For a given numerical grid, the smallest pore radius is approximated by the grid-spacing Δx, leading to a maximum pressure of

$$p_{\Delta x} = \frac{2\sigma}{\Delta x}. \tag{B.2}$$

The behavior changes, if the grains in the porous medium are not connected anymore. If there are at least two lattice spacing between two geometric objects, film flow breaks and it is possible to obtain a residual water saturation. An approximate method to compute the irreducible wetting phase saturation is given in [65], page 205 ff, if the irreducible wetting phase exists in form of liquid bridges and the porous medium is composed of spheres. The value of the residual saturation S_r can be computed, by referring to Schubert [65, p. 207, Table 4.2], and using linear interpolation. The related capillary pressure $p_{c,res}$ can be obtained by again referring to Schubert [65, p. 128, Fig. 4.12]. We used a body centered cubic array of spheres,
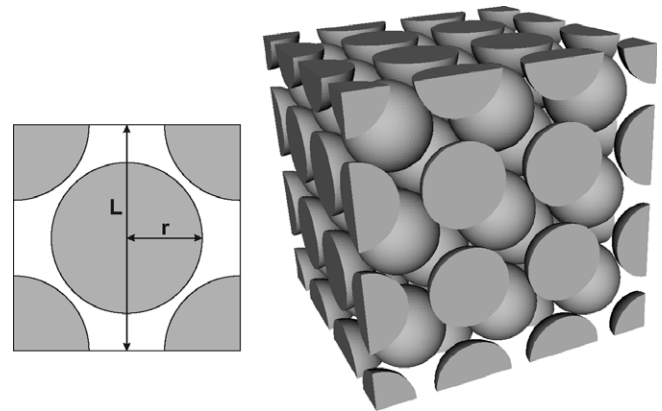

Fig. B.8. Body centered array of spheres, left: geometric relations, right: simulation domain.

shown in Fig. B.8 to test this behavior. The porosity ϕ can be computed from

$$\phi = 1 - \frac{8\pi r^3}{3L^3} \tag{B.3}$$

and the closest distance a of two spheres from

$$\frac{a}{2r} = \frac{\sqrt{3}L}{4r} - 1. \tag{B.4}$$

Two setups given in Table B.1 have been tested. The material parameters have been $\mu_w = 1/200$ Pa s, $\mu_n = 1/500$ Pa s, $\sigma = 0.01$ N m^{-1} and the driving capillary pressure was increased linearly over time up to a maximum value of approximately $p_{max} = 18\sigma/(2r)$. The material parameters had the same values as we have used for the simulations in real porous media carried out in Section 4.3. The domain was initially filled with a wetting

Table B.1
Residual saturation, approximation by Schubert and the LB simulation

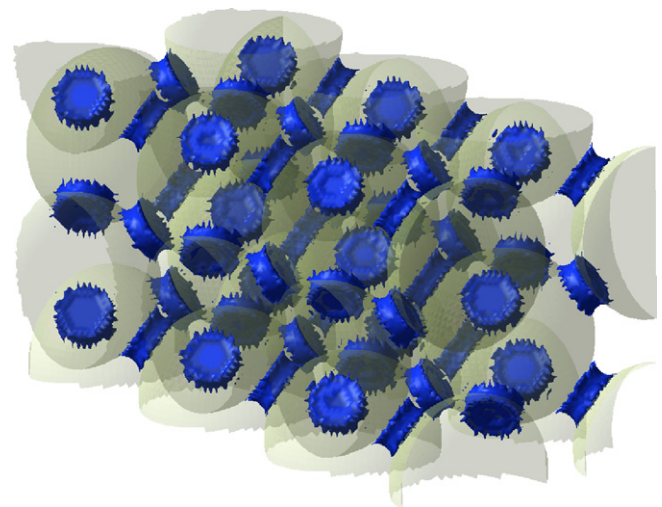|	$\frac{a}{2r}$	ϕ	$\frac{p_{c,res}2r}{\sigma}$, Schubert	S_r, Schubert	S_r, LB
Setup 1	0.0	0.32	≈ 9	0.06	0.0 (film flow)
Setup 2	0.083	0.46	≈ 4	0.12	0.13

Fig. B.9. Irreducible wetting phase saturation for setup 2.

phase and then drained by the increasing pressure. The grid resolution was 150^3, so that one sphere is resolved by approximately 40 grid points. In the first case the medium is drained almost completely, whereas in the second case we obtain a residual saturation of 0.13. The distribution of the non-wetting phase (NWP) is shown in Fig. B.9. The values of setup 2 are very close and indicate the validity of the approach. Nevertheless further investigation has to be done and is beyond the scope of this paper.

For a general porous medium obtained by tomography methods it is very difficult to estimate the irreducible NWP saturation by lattice Boltzmann methods, since the medium is generally con-

nected and the individual grains are not known. A method to identify single items in the structure is described in [22]. A possible future direction to estimate the irreducible NWP saturation by LB methods could use these methods and shrink the single items by two voxel layers in the numerical simulation grid. Finally one has to do several simulation runs on successively refined grids, always keeping a distance of two voxel layers between the single items, until a convergent behavior is observed. Nevertheless this is a very demanding simulation setup.

Appendix C. Transformation matrix M

$$
M = \begin{bmatrix}
1\cdot & (1 & 1 & 1 & 1 & 1 & 1 & 1 & 1 & 1 & 1 & 1 & 1 & 1 & 1 & 1 & 1 & 1 & 1 & 1) \\
c^2\cdot & (-1 & 0 & 0 & 0 & 0 & 0 & 0 & 1 & 1 & 1 & 1 & 1 & 1 & 1 & 1 & 1 & 1 & 1 & 1) \\
c^4\cdot & (1 & -2 & -2 & -2 & -2 & -2 & -2 & 1 & 1 & 1 & 1 & 1 & 1 & 1 & 1 & 1 & 1 & 1 & 1) \\
c\cdot & (0 & 1 & -1 & 0 & 0 & 0 & 0 & 1 & -1 & 1 & -1 & 1 & -1 & 1 & -1 & 0 & 0 & 0 & 0) \\
c^3\cdot & (0 & -2 & 2 & 0 & 0 & 0 & 0 & 1 & -1 & 1 & -1 & 1 & -1 & 1 & -1 & 0 & 0 & 0 & 0) \\
c\cdot & (0 & 0 & 0 & 1 & -1 & 0 & 0 & 1 & -1 & -1 & 1 & 0 & 0 & 0 & 0 & 1 & -1 & 1 & -1) \\
c^3\cdot & (0 & 0 & 0 & -2 & 2 & 0 & 0 & 1 & -1 & -1 & 1 & 0 & 0 & 0 & 0 & 1 & -1 & 1 & -1) \\
c\cdot & (0 & 0 & 0 & 0 & 0 & 1 & -1 & 0 & 0 & 0 & 0 & 1 & -1 & -1 & 1 & 1 & -1 & -1 & 1) \\
c^3\cdot & (0 & 0 & 0 & 0 & 0 & -2 & 2 & 0 & 0 & 0 & 0 & 1 & -1 & -1 & 1 & 1 & -1 & -1 & 1) \\
c^2\cdot & (0 & 2 & 2 & -1 & -1 & -1 & -1 & 1 & 1 & 1 & 1 & 1 & 1 & 1 & 1 & -2 & -2 & -2 & -2) \\
c^4\cdot & (0 & -2 & -2 & 1 & 1 & 1 & 1 & 1 & 1 & 1 & 1 & 1 & 1 & 1 & 1 & -2 & -2 & -2 & -2) \\
c^2\cdot & (0 & 0 & 0 & 1 & 1 & -1 & -1 & 1 & 1 & 1 & 1 & -1 & -1 & -1 & -1 & 0 & 0 & 0 & 0) \\
c^4\cdot & (0 & 0 & 0 & -1 & -1 & 1 & 1 & 1 & 1 & 1 & 1 & -1 & -1 & -1 & -1 & 0 & 0 & 0 & 0) \\
c^2\cdot & (0 & 0 & 0 & 0 & 0 & 0 & 0 & 1 & 1 & -1 & -1 & 0 & 0 & 0 & 0 & 0 & 0 & 0 & 0) \\
c^2\cdot & (0 & 0 & 0 & 0 & 0 & 0 & 0 & 0 & 0 & 0 & 0 & 0 & 0 & 0 & 0 & 1 & 1 & -1 & -1) \\
c^2\cdot & (0 & 0 & 0 & 0 & 0 & 0 & 0 & 0 & 0 & 0 & 0 & 1 & 1 & -1 & -1 & 0 & 0 & 0 & 0) \\
c^3\cdot & (0 & 0 & 0 & 0 & 0 & 0 & 0 & 1 & -1 & 1 & -1 & -1 & 1 & -1 & 1 & 0 & 0 & 0 & 0) \\
c^3\cdot & (0 & 0 & 0 & 0 & 0 & 0 & 0 & -1 & 1 & 1 & -1 & 0 & 0 & 0 & 0 & 1 & -1 & 1 & -1) \\
c^3\cdot & (0 & 0 & 0 & 0 & 0 & 0 & 0 & 0 & 0 & 0 & 0 & 1 & -1 & -1 & 1 & -1 & 1 & 1 & -1)
\end{bmatrix}
$$

Appendix D. Estimated parameters for the inverse fit

See Tables D.1, D.2 and D.3.

Table D.1
Estimated parameters for the primary drainage branch – column 1/2

Parameter		Unit			Measured
ρ_b		kg m^{-3}			1567/1563
ϕ[a]		–			0.409/0.410
K_s		m^2			4.09E−11/1.94E−11
θ_s		–			0.396/0.385

		Estimated			
		vG cons	vG uncons	vG bimod	ff
α_1	Pa^{-1}	3.39E−04/3.34E−04	3.64E−04/3.36E−04	3.37E−04/3.31E−04	–
n_1	–	11.42/10.91	15.13/11.05	12.77/12.04	–
m_1	–	$=1-1/n_1$	0.479/0.870	$=1-1/n_1$	–
θ_r	–	0.076/0.070	0.070/0.070	0.072/0.073	–
α_2	Pa^{-1}	–	–	7.77E−04/1.09E−03	–
n_2	–	–	–	1.87/4.93	–
m_2	–	–	–	$=1-1/n_2$	–
w_2	–	–	–	0.061/0.032	–
τ	–	0.625/0.370	1.039/0.408	0.902/0.216	–
RMSE$_p$[b]	Pa	5.86E+01/2.68E+01	5.64E+01/2.67E+01	5.73E+01/2.83E+01	5.66E+01/3.20E+01
RMSE$_Q$[c]	m	4.18E−04/3.53E−04	3.95E−04/3.53E−04	3.42E−04/2.21E−04	2.04E−04/7.56E−05

[a] Calculated assuming $\rho_s = 2650$ kg m^{-3}: $\phi = 1 - \rho_b/\rho_s$.
[b] Root mean square error of the measurement and model prediction of capillary pressure, *p*.
[c] Root mean square error of the measurement and model prediction of cumulative outflow, *Q*.

Table D.2
Estimated parameters for the first imbibition branch – column 1/2

Parameter		Unit				Measured
ρ_b		kg m^{-3}				1567/1563
ϕ[a]		–				0.409/0.410
K_s		m^2				4.09E−11/1.94E−11
θ_s		–				0.351/0.343
		Estimated				
		vG cons	vG uncons	vG bimod	ff	
α_1	Pa^{-1}	6.57E−04/5.67E−04	6.41E−04/ 7.01E−04	6.13E−04[b]/4.96E−04	–	
n_1	–	14.45/4.93	13.22/8.34	15.0[b]/10.28	–	
m_1	–	=1 − 1/n_1	1.031/0.278	=1 − 1/n_1	–	
θ_r	–	0.075/0.063	0.074/0.055	0.0[b]/0.027	–	
α_2	Pa^{-1}	–	–	4.60E−03/9.00E−04	–	
n_2	–	–	–	1.10/1.97	–	
m_2	–	–	–	=1 − 1/n_2	–	
w_2	–	–	–	0.366/0.457	–	
τ	–	1.606/1.084	1.031/2.0[b]	2.0[b]/2.0[b]	–	
RMSE$_p$[c]	Pa	5.24E+02/1.87E+02	5.40E+02/1.50E+02	2.04E+02/6.39E+01	7.53E+01/3.05E+01	
RMSE$_Q$[d]	m	9.32E−04/4.75E−04	9.09E−04/5.31E−04	7.86E−04/2.18E−04	5.02E−04/9.27E−05	

[a] Calculated assuming ρ_s = 2650 kg m^{-3}: $\phi = 1 − \rho_b/\rho_s$.
[b] Estimated parameter reached boundary of parameter space.
[c] Root mean square error of the measurement and model prediction of capillary pressure, p.
[d] Root mean square error of the measurement and model prediction of cumulative outflow, Q.

Table D.3
Estimated parameters for the secondary drainage branch – column 1/2

Parameter		Unit				Measured
ρ_b		kg m^{-3}				1567/1563
ϕ[a]		–				0.409/0.410
K_s		m^2				4.09E−11/1.94E−11
θ_s		–				0.351/0.343
		Estimated				
		vG cons	vG uncons	vG bimod	ff	
α_1	Pa^{-1}	3.45E−04/3.43E−04	3.18E−04/ 3.41E−04	3.39E−04/3.39E−04	–	
n_1	–	8.02/8.77	7.15/8.66	9.47/9.90	–	
m_1	–	=1 − 1/n_1	1.37/0.93	=1 − 1/n_1	–	
θ_r	–	0.062/0.061	0.068/0.062	0.0625/0.064	–	
α_2	Pa^{-1}	–	–	6.87E−04/1.53E−03	–	
n_2	–	–	–	2.28/2.35	–	
m_2	–	–	–	=1 − 1/n_2	–	
w_2	–	–	–	0.097/0.046	–	
τ	–	1.380/0.783	1.018/0.744	1.315/0.561	–	
RMSE$_p$[b]	Pa	5.64E+01/3.38E+01	5.80E+01/ 3.39E+01	5.57E+01/3.38E+01	5.61E+01/3.71E+01	
RMSE$_Q$[c]	m	3.04E−04/3.34E−04	2.86E−04/ 3.34E−04	1.63E−04/2.04E−04	1.36E−04/1.11E−04	

[a] Calculated assuming ρ_s = 2650 kg m^{-3}: $\phi = 1 − \rho_b/\rho_s$.
[b] Root mean square error of the measurement and model prediction of capillary pressure, p.
[c] Root mean square error of the measurement and model prediction of cumulative outflow, Q.

Appendix E. Measured data and model fits
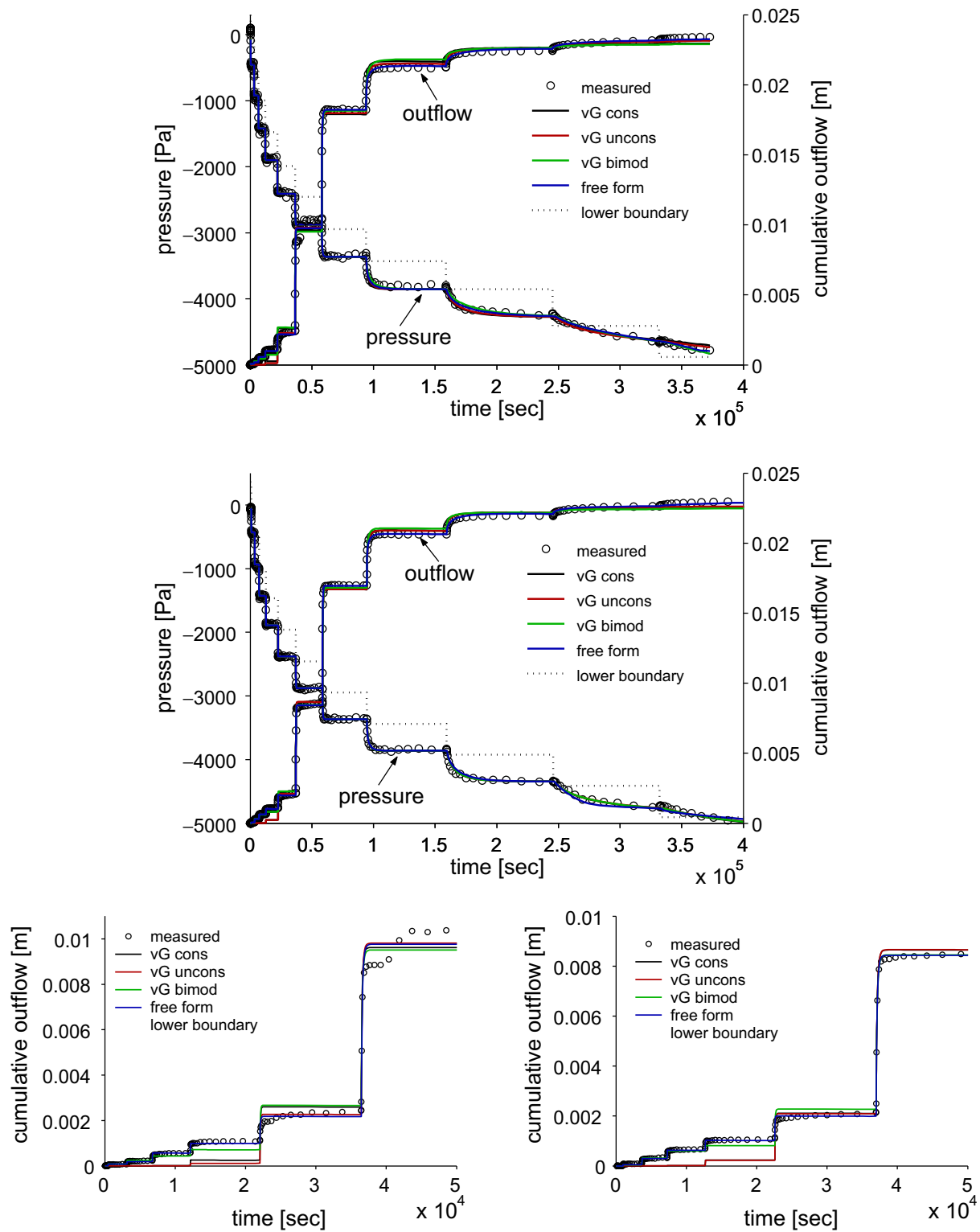
See Figs. E.1, E.2 and E.3.

Fig. E.1. Primary drainage branch: measured data and fitted with four different hydraulic properties models. Top: matric head and cumulative outflow for column 1; Middle: matric head and cumulative outflow for column 2; Bottom: cumulative outflow for column 1 (left) and 2 (right) for $h_{LB} \geqslant -25$ to show the better performance of the more flexible models.
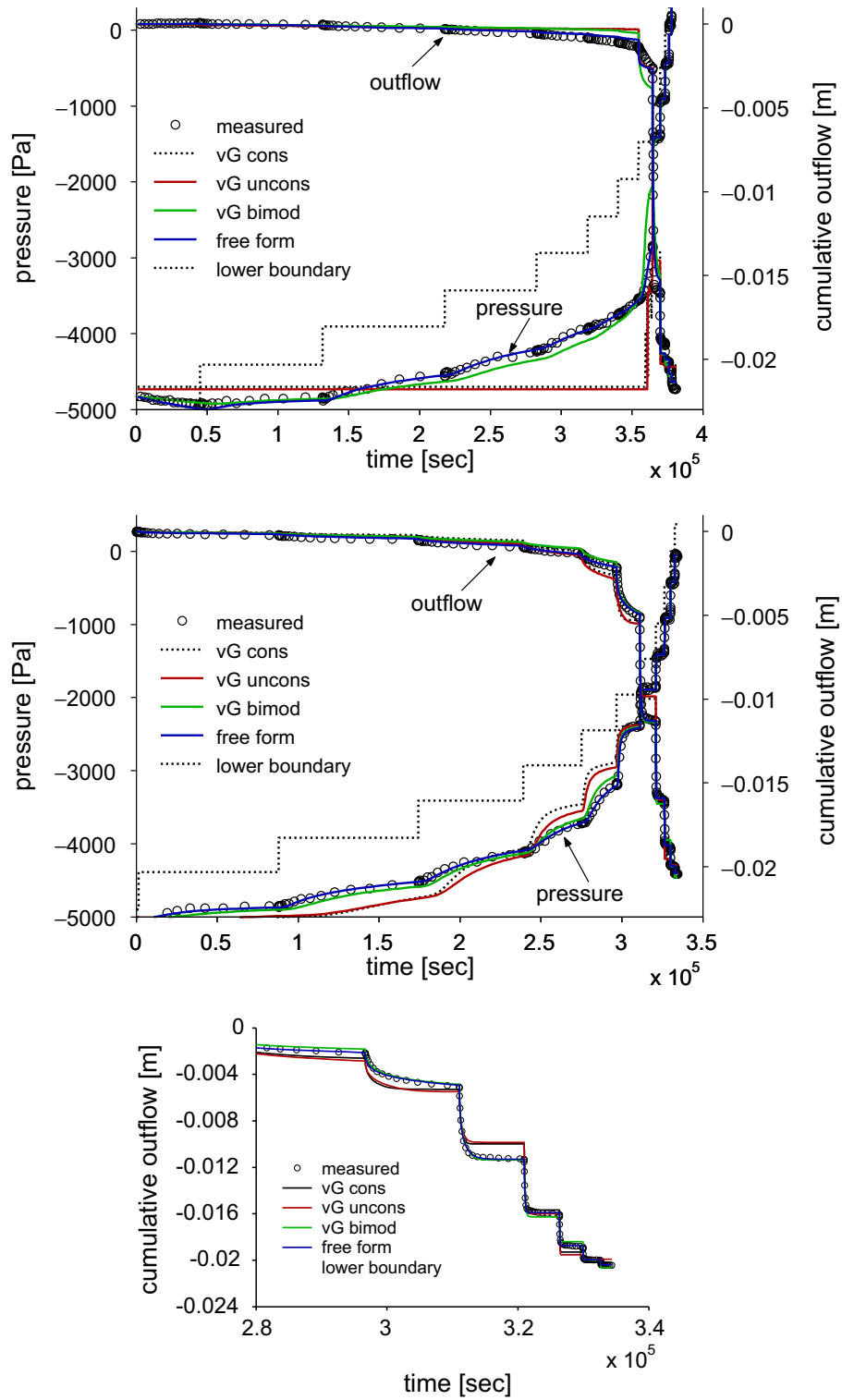
Fig. E.2. First imbibition branch: measured data and fitted with four different hydraulic properties models. Top: matric head and cumulative outflow for column 1; middle: matric head and Cumulative outflow for column 2; bottom: cumulative outflow for column 2 for $h_{LB} \geqslant -25$ to show the better performance of the more flexible models.
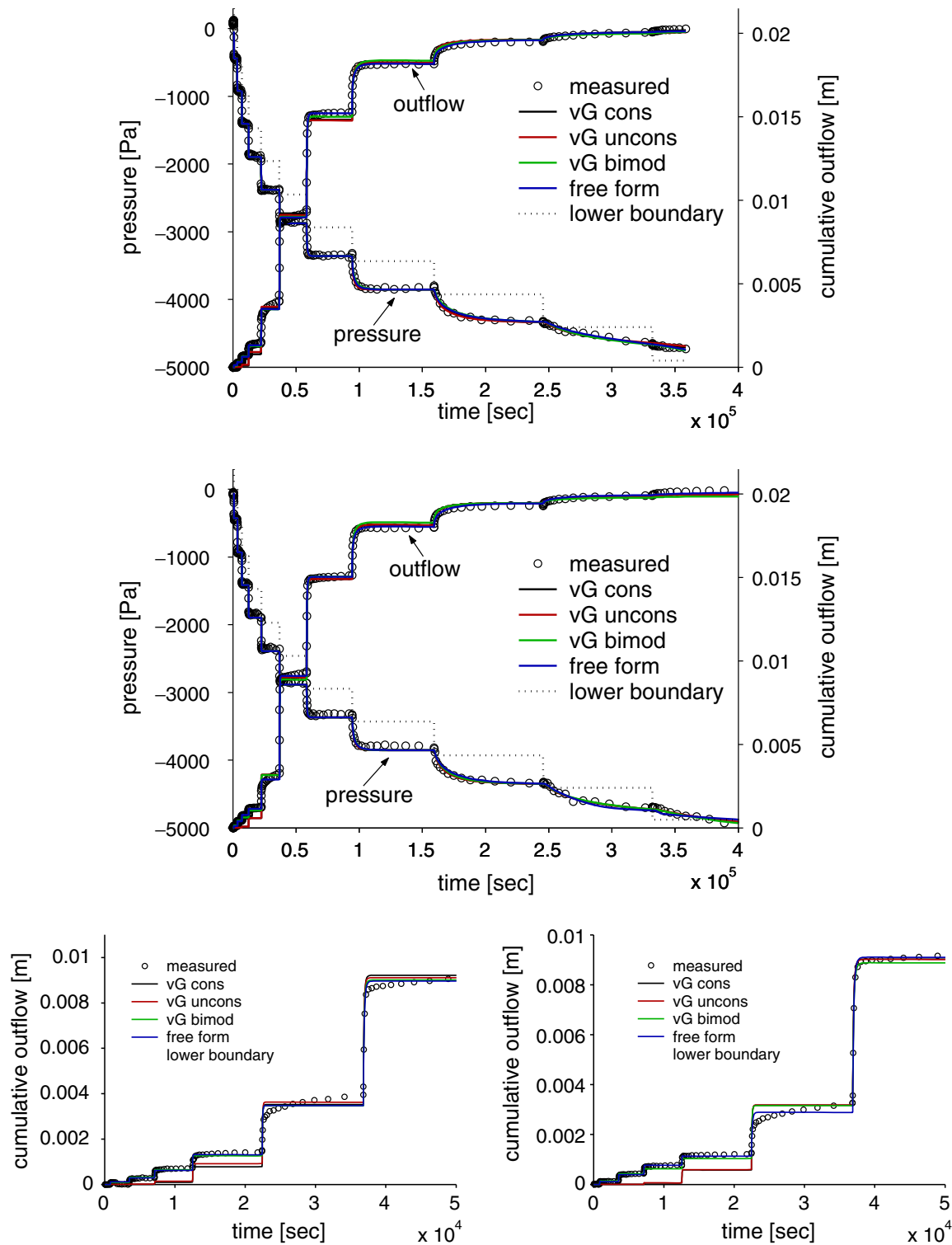
Fig. E.3. Secondary drainage branch: Measured data and fitted with four different hydraulic properties models. Top: matric head and cumulative outflow for column 1; middle: matric head and cumulative outflow for column 2; bottom: cumulative outflow for column 1 (left) and 2 (right) $h_{LB} \geqslant -25$ to show the better performance of the more flexible models.

References

[1] Tölke J, Freudiger S, Krafczyk M. An adaptive scheme for LBE multiphase flow simulations on hierarchical grids. Comput Fluids 2006;35:820–30.

[2] Haines W. Studies in the physical properties of soils: V. The hysteresis effect in capillary properties, and the modes of moisture distribution associated therewith. J Agri Sci 1930;20:97–116.

[3] Moseley W, Dhir VK. Capillary pressure–saturation relationship in porous media including the effect of wettability. J Hydrol 1996;178:33–53.

[4] Lehmann P, Stauffer F, Hinz C, Dury O, Flühler H. Effect of hysteresis on water flow in sand column with a fluctuating capillary fringe. J Contam Hydrol 1998;33:81–100.

[5] Russo D, Jury W, Butters G. Numerical analysis of solute transport during transient irrigation: 1. The effect of hysteresis and profile heterogeneity. Water Resource Res 1989;25:2109–18.

[6] Mualem Y. A conceptual model of hysteresis. Water Resour Res 1974;10:514–20.

[7] Kool J, Parker J. Development and evaluation of closed-form expressions for hysteretic soil hydraulic properties. Water Resour Res 1987;23:105–14.

[8] Huang H-C, Tan Y-C, Liu C-W, Chen C-H. A novel hysteresis model in unsaturated soils. Hydrol Process 2005;19:1653–65.

[9] Mualem Y. Extension of the similarity hypothesis used for modeling soil water characteristics. Water Resour Res 1977;13:773–80.

[10] O'Kane J, Flynn D. Thresholds switches and hysteresis in hydrology from the pedon to the catchment scale: a non-linear systems theory. Hydrol Earth Syst Sci 2007;11:443–59.

[11] Hilfer R. Macroscopic capillarity and hysteresis for flow in porous media. Phys Rev E 2006;73:016307.

[12] Jerauld G, Salter S. The effect of pore-structure on hysteresis in relative permeability and capillary pressure: pore-level modeling. Transp Porous Media 1989;5:103–51.

[13] Held R, Celia M. Modeling support of functional relationships between capillary pressure, saturation, interfacial area and common lines. Adv Water Res 2001;24:325–43.

[14] Vidales A, Faccio R, Zgrablich G. Capillary hysteresis in porous media. J Phys: Cond Mat 1995;7:3835–43.

[15] Øren P-E, Bakke S, Arntzen OJ. Extending predictive capabilities to network models. SPE J 1998;3:324–36.

[16] Valvatne P, Piri M, Lopez X, Blunt M. Predictive pore-scale modeling of single and multiphase flow. Transp Porous Media 2005;58:23–41.

[17] Pan C, Hilpert M, Miller CT. Lattice-Boltzmann simulation of two-phase flow in porous media. Water Resour Res 2004;40:W01501.

[18] Shan X, Chen H. Lattice Boltzmann model for simulating flows with multiple phases and components. Phys Rev E 1993;47:1815–9.

[19] Li H, Pan C, Miller C. Pore-scale investigation of viscous coupling effects for two-phase flow in porous media. Phys Rev E 2005;72:026705.

[20] Vogel H-J, Tölke J, Schulz VP, Krafczyk M, Roth K. Comparison of a lattice-Boltzmann model, a full-morphology model, and a pore network model for determining capillary pressure–saturation relationships. Vadose Zone J 2005;4(2):380–8.

[21] Ahrenholz B, Tölke J, Krafczyk M. Lattice-Boltzmann simulations in reconstructed parametrized porous media. Int J Comput Fluid Dyn 2006;20(6):369–77.

[22] Kaestner A, Lehmann E, Stampanoni M. Imaging and image processing in soil science. Adv Water Res 2008;31(9):1174–87.

[23] Zurmühl T. Capability of convection dispersion transport models to predict transient water and solute movement in undisturbed soil columns. J Contam Hydrol 1998;30:99–126.

[24] van Genuchten MT. A closed-form equation for predicting the hydraulic conductivity of unsaturated soils. Soil Sci Soc Am J 1980;44:892–8.

[25] Durner W. Hydraulic conductivity estimation for soils with heterogeneous pore structure. Water Resour Res 1994;30:211–23.

[26] Bitterlich S, Durner W, Iden SC, Knabner P. Inverse estimation of the unsaturated soil hydraulic properties from column outflow experiments using free-form parameterizations. Vadose Zone J 2004;3:971–81.

[27] Mualem Y. A new model for predicting the hydraulic conductivity of unsaturated porous media. Water Resour Res 1976;12(3):513–21.

[28] Priesack E, Durner W. Closed form expression for the multi-modal unsaturated conductivity function. Vadose Zone J 2006;5:121–4.

[29] Duan Q, Sorooshian S, Gupta V. Effective and efficient global optimization for conceptual rainfall-runoff models. Water Resour Res 1992;28:1015–31.

[30] Peters A, Durner W. Improved estimation of soil water retention characteristics from hydrostatic column experiments. Water Resour Res 2006;42(11):W11401.

[31] Hilpert M, Miller C. Pore-morphology-based simulation of drainage in totally wetting porous media. Adv Water Res 2001;243–55.

[32] Lehmann P, Wyss P, Flisch A, Lehmann E, Vontobel P, Krafczyk M, et al. Tomographical imaging and mathematical description of porous media used for the prediction of fluid distribution. Vadose Zone J 2006;5:80–97.

[33] Rothman DH, Keller JM. Immiscible cellular automaton fluids. J Stat Phys 1988;52:1119–27.

[34] Gunstensen A, Rothman D. Lattice Boltzmann model of immiscible fluids. Phys Rev A 1991;43(8):4320–7.

[35] Grunau D, Chen S, Eggert K. A lattice Boltzmann model for multiphase fluid flows. Phys Fluids A: Fluid Dyn 1993;5(10):2557–62.

[36] Swift MR, Osborn WR, Yeomans JM. Lattice Boltzmann Simulation of Nonideal Fluids. Phys Rev Lett 1995;75(5):830–3.

[37] Luo L-S. Unified theory of the lattice Boltzmann models for nonideal gases. Phys Rev Lett 1998;81(8):1618–21.

[38] Bouzidi M, Firdaouss M, Lallemand P. Momentum transfer of a Boltzmann-Lattice fluid with boundaries. Phys Fluids 2001;13(11):3452–9.

[39] Lallemand P, Luo L-S. Lattice Boltzmann method for moving boundaries. J Comput Phys 2003;184:406–21.

[40] Tölke J. Gitter–Boltzmann–Verfahren zur Simulation von Zweiphasenströmungen, PhD thesis, TU München; 2001.

[41] MPI-Forum, Message passing interface; 2006. <http://www.mpi-forum.org>.

[42] Lewiner T, Lopes H, Vieira AW, Tavares G. Efficient implementation of Marching Cubes' cases with topological guarantees. J Graph Tools 2003;8(2):1–15.

[43] Kozeny J. Über kapillare Leitung des Wassers im Boden – Aufstieg, Versickerung und Anwendung auf die Bewässerung, Sitzungsberichte Akademie der Wissenschaften Wien. Abt IIa 1927;136:271–306.

[44] Martys N, Chen H. Simulation of multicomponent fluids in complex three-dimensional geometries by the lattice Boltzmann method. Phys Rev E 1996;53:743–50.

[45] Adler PM, Thovert FF. Real porous media: local geometry and macroscopic properties. Appl Mech Rev 1998;51(9):537–85.

[46] Yang ZL, Dinh TN, Nourgaliev RR, Sehgal BR. Evaluation of the Darcys law performance for two-fluid flow hydrodynamics in a particle debris bed using a lattice-Boltzmann model. Heat Mass Transfer 2000;36:295–304.

[47] Tölke J, Krafczyk M, Schulz M, Rank E. Lattice Boltzmann simulations of binary fluid flow through porous media. Phil Trans Royal Soc A – Math, Phys Eng Sci 2002;360(1792):573–91.

[48] Bekri S, Vizikab O, Thovert J-F, Adler P. Binary two-phase flow with phase change in porous media. Int J Multiphase Flow 2001;27:477–526.

[49] Adler PM, Thovert J-F, Bekri S, Yousefian F. Real porous media: local geometry and transports. J Eng Mech (ASCE) 2002;128(8):829–39.

[50] Bekri S, Adler PM. Dispersion in multiphase flow through porous media. Int J Multiphase Flow 2002;28:665–97.

[51] Bekri S, Howard J, Muller J, Adler PM. Electrical resistivity index in multiphase flow through porous media. Transp Porous Media 2003;51:41–65.

[52] Lehmann P, Krafczyk M, Gygi A, Flisch A, Wyss P, Flühler H. Modelling flow of water and air in reconstructed structures of porous media. In: Proceedings of the second world congress on industrial tomography, Hannover; 2001. p. 628–35.

[53] Washburn EW. The dynamics of capillary flow. Phys Rev 1921;17(3):273–83.

[54] Piri M, Blunt MJ. Three-dimensional mixed-wet random pore-scale network modeling of two- and three-phase flow in porous media. I. Model description. Phys Rev E 2005;71:026301.

[55] Piri M, Blunt MJ. Three-dimensional mixed-wet random pore-scale network modeling of two- and three-phase flow in porous media. II. Results. Phys Rev E 2005;71:026302.

[56] Frisch U, d'HumiFres D, Hasslacher B, Lallemand P, Pomeau Y, Rivet J-P. Lattice gas hydrodynamics in two and three dimensions. Comp Syst 1987:75–136.

[57] Benzi R, Succi S, Vergassola M. The lattice Boltzmann equation: theory and applications. Phys Rep 1992;222(3):147–97.

[58] Chen S, Doolen G. Lattice Boltzmann method for fluid flows. Annu Rev Fluid Mech 1998;30:329–64.

[59] Qian YH, d'Humières D, Lallemand P. Lattice BGK models for Navier–Stokes equation. Europhys Lett 1992;17:479–84.

[60] Kehrwald D. Numerical analysis of immiscible lattice BGK, PhD thesis, Universität Kaiserslautern; 2003.

[61] d'Humières D. Generalized lattice-Boltzmann equations. in: Shizgal BD, Weave DP, editors, Rarefied gas dynamics: theory and simulations, Prog Astronaut Aeronaut, vol. 159. AIAA, Washington DC; 1992. p. 450–58.

[62] Lallemand P, Luo L-S. Theory of the lattice Boltzmann method: dispersion, dissipation, isotropy, Galilean invariance, and stability. Phys Rev E 2000;61(6):6546–62.

[63] Ginzburg I. Variably saturated flow with the anisotropic lattice Boltzmann method. Comput Fluids 2006;35(8/9):831–48.

[64] Junk M, Klar A, Luo L-S. Asymptotic analysis of the lattice Boltzmann equation. J Comput Phys 2005;210(2):676–704.

[65] Schubert H. Kapillarität in porösen Feststoffsystemen. Springer-Verlag; 1982, ISBN 3-540-11835-7.